

Fall 2016

## Physical Properties of Traditional and Water-Miscible Oil Paints as Assessed By Single-Sided Nmr

Nicholas Anthony Sanchez Udell

College of William and Mary - Arts & Sciences, [naudell@email.wm.edu](mailto:naudell@email.wm.edu)

Follow this and additional works at: <https://scholarworks.wm.edu/etd>

 Part of the [Chemistry Commons](#)

---

### Recommended Citation

Udell, Nicholas Anthony Sanchez, "Physical Properties of Traditional and Water-Miscible Oil Paints as Assessed By Single-Sided Nmr" (2016). *Dissertations, Theses, and Masters Projects*. Paper 1499449865. <http://doi.org/10.21220/S23950>

This Thesis is brought to you for free and open access by the Theses, Dissertations, & Master Projects at W&M ScholarWorks. It has been accepted for inclusion in Dissertations, Theses, and Masters Projects by an authorized administrator of W&M ScholarWorks. For more information, please contact [scholarworks@wm.edu](mailto:scholarworks@wm.edu).

Physical Properties of Traditional and Water-Miscible Oil Paints as assessed by Single-sided NMR

Nicholas Anthony Sanchez Udell

Warrenton, VA

B.S. Chemistry, The College of William and Mary, 2015

A Thesis presented to the Graduate Faculty  
of the College of William and Mary in Candidacy for the Degree of  
Master of Science

Chemistry

The College of William and Mary  
January, 2017

© Copyright by Nicholas A. S. Udell 2016

## APPROVAL PAGE

This Thesis is submitted in partial fulfillment of  
the requirements for the degree of

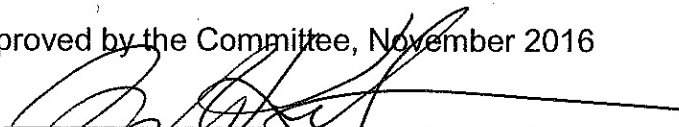
Master of Science



---

Nicholas Anthony Sanchez Udell

Approved by the Committee, November 2016



---

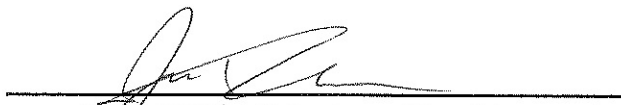
Committee Chair

Assistant Professor Tyler Meldrum, Chemistry  
College of William and Mary



---

Professor Deborah Bebout, Chemistry  
College of William and Mary



---

Professor John C. Poutsma, Chemistry  
College of William and Mary

## ABSTRACT

Single-sided NMR has been demonstrated as a useful technique for the inexpensive and non-invasive study of cultural heritage objects, including numerous different painting and paint samples. The relatively recent invention of water-miscible oil paints – a new form of environmentally friendly oil paint that can be thinned and cleaned by water – provides a need for analysis of the physical properties of the cured paint films. Single-sided NMR offers an excellent analytical tool to study the structural effects of the emulsifying agent present in water-miscible oil paints on the paint linoxyn network by measuring the transverse ( $T_2$ ) relaxation times for various pigments. In this research, single-sided NMR is shown to be a successful technique in analyzing the physical properties of oil paint networks in comparison to the chemical composition of the paints as assessed by fatty acid ratios derived from complimentary GCMS data. The discovery of a correlation between specific fatty acid ratios and relaxation times suggests that the presence of the emulsifying agent interferes with autoxidation and the cross-linking of the paint network, impeding the relative rate of curing. The conclusions drawn from this research offer the potential for multiple new experiments to better understand the chemistry behind the curing of oil paints in the presence of an emulsifying agent.

## TABLE OF CONTENTS

Acknowledgements	ii
List of Tables	iii
List of Figures	iv
Chapter 1. Introduction	1
Chapter 2. Background	5
Chapter 3. Experimental	29
Chapter 4. Results and Discussion	42
Chapter 5. Conclusions	48
Appendices	51
Bibliography	67

## ACKNOWLEDGEMENTS

This writer wishes to express his appreciation to Professor Tyler Meldrum, under whose guidance this investigation was conducted, for his patience, guidance and criticism throughout the investigation. Furthermore, this writer would like to thank Professor Meldrum for believing in him and giving him the opportunity to grow and learn as a scientist under his tutelage. The author is also indebted to Professors Poutsma and Bebout for their careful reading and criticism of the manuscript.

This writer would also like to thank the Office of Graduate Studies and Research for graduate student research grant support, as well as the College of William and Mary Graduate Studies Advisory Board for fellowship funding.

## LIST OF TABLES

1. Profile Experimental Parameters	51
2. CPMG Experimental Parameters	53
3. Sample Group A Data	55
4. Sample Group B Data	56
5. Sample Group C WMO Data (M001 – M095)	57
6. Sample Group C WMO Data (M205 – M232)	58
7. Sample Group C TO Data (P001 – P095)	59
8. Sample Group C TO Data (P205 – P250)	60
9. Sample Group D Data	61



## LIST OF FIGURES

1. Structure of Emulsifying Agent Atlas G-1086	3
2. Visualization of the Three-Dimensional Bulk Magnetization Vector	7
3. Precession in a Conical Fashion About the Z-Axis	9
4. Magnetization Being Shifted from the Z-Axis to the XY-Plane	11
5. The Basic Pulse-Acquisition Experiment	12
6. Cross-sectional Representation of the NMR-MOUSE	14
7. Diagram of a Hahn Echo	17
8. The Refocusing of Individual Magnetic Moments	18
9. The CPMG Pulse Sequence	19
10. Cross-linking Between Adjacent Glyceride Chains	25
11. A Mechanism for the Formation of Cross-linkages	26
12. A Mechanism for the Formation of Azelaic Acid via $\beta$ -scission	28
13. Example Images of Samples Measured	32
14. Image of the NMR-MOUSE Apparatus	35
15. Sample Profile Experiments	37
16. A Sample Echo Train	38
17. A Sample Residual Plot	41
18. Graph of Relaxation Times vs O/P and A/P Fatty Acid Ratios for Sample Group B	43
19. Graph of Relaxation Time vs the Curing Time for Sample Group C	44
20. Graph of Relaxation Times vs O/P and A/P Fatty Acid Ratios for Sample Group A	46
21. Graph of Relaxation Times vs O/P and A/P Fatty Acid Ratios for Sample Group D	47

22. Supplementary Figure of Profile Parameters in Prospa Software	52
23. Supplementary CPMG of Profile Parameters in Prospa Software	54

## **Chapter 1: Introduction**

### *Single-Sided NMR*

Traditional nuclear magnetic resonance (NMR) spectroscopy is a well-known technique with years of documented applications in the commercial, medical, and research fields.<sup>1</sup> Traditional NMR entails utilizing large stationary magnets containing superconducting components in order to analyze samples with applied radio-waves. Single-sided nuclear magnetic resonance is an alternative NMR analysis method that came into prominence in the mid 1990's, concurrent with the invention of hardware capable of producing applied magnetic fields strong enough for analysis while still being light weight enough to enable portability. As opposed to traditional NMR, which can produce magnetic fields on the order of tens of Tesla ( $T$ ) with radiofrequencies on the order of hundreds of MHz, single-sided NMR utilizes mobile apparatuses which produce magnetic fields with radiofrequencies that are orders of magnitude weaker.<sup>2</sup> Nevertheless, single-sided NMR is now a well-documented technique used across multiple fields of research and industry. Single-sided NMR allows for the non-invasive study of objects and chemical processes, including: oil wells,<sup>3,4</sup> food,<sup>5-7</sup> manufacturing processes,<sup>8</sup> paintings,<sup>9-13</sup> instruments,<sup>14</sup> ceramics,<sup>15</sup> paper,<sup>16,17</sup> and building materials.<sup>18</sup>

Single-sided NMR utilizes permanent magnets that require no superconducting material; this, in turn, greatly reduces engineering and operation complications associated with traditional NMR equipment. Conversely, the permanent block magnets utilized in single-sided NMR are incapable of producing a homogenous magnetic field, instead utilizing weaker, inhomogeneous magnetic fields. These weaker, inhomogeneous fields, while still serviceable, provide less signal to work than traditional

NMR magnets. Single-sided NMR is spatially smaller than traditional NMR, and its open geometry removes the need for invasive sample preparation. These attributes not only provide greater portability for single-sided NMR, but also allow data collection at a fraction of the cost of homogenous NMR. Because single-sided NMR instruments benefit from unique geometries and portability, they are well-suited for the analysis of planar samples, including paints and paintings, that may otherwise require invasive means to analyze. These magnets can also be brought to the museum or gallery, rather than bringing the art to the lab. For these reasons, and others, this research sought to utilize single-sided NMR for art-related goals. In addition, the small size of the single-sided magnets allows them to be mounted on mechanical lifts that can control motion of the entire magnet arrangement. This facilitates NMR “profiling” or one-dimensional imaging of paint layers with resolution on the scale of tens of microns.<sup>19</sup> By utilizing the Carr-Purcell-Meiboom-Gill (CPMG) pulse sequence,<sup>20</sup> effective spin-spin relaxation times ( $T_2$ ) can be determined, while also overcoming complications attributed to the field inhomogeneity of the single-sided apparatus.<sup>21</sup> The relaxation times relate to the stiffness or rigidity of a material, as smaller values of  $T_2$  indicate material with restricted intermolecular motion due to greater molecular cross-linking.<sup>22</sup> In a paint film, a decrease in intermolecular motion (or, equivalently, in  $T_2$ ) correlates with oxidation of a paint film, due to the cross-linking that occurs during oxidation. Experimentally obtained  $T_2$  values are dependent on measurement parameters and therefore cannot provide absolute information on a given system. However, CPMG measurements obtained using identical parameters can be used to make comparisons among samples. This methodology was applied in lab in order to measure numerous paint samples of

interest.

### *Water-Miscible Oil Paints*

Water-miscible oil paints (WMOs) are a relatively new form of oil paint that can be both cleaned and thinned by water. WMOs not only benefit from the reduced costs associated with water solubility, but also provide an environmentally friendly alternative to traditional counterparts that require chemical solvents to clean and thin. WMOs are similar in composition to traditional oil paints (TOs), but derive their water miscibility from an emulsifying agent, for example polyethoxyethylene sorbitol hexaoleate, diagrammed in Figure 1, composed of a hydrophobic tails and a hydrophilic center. The hydrophilic center allows for uptake of water into the paint, while the hydrophobic tail can integrate with the oil, creating a stable paint emulsion consisting of a water-in-oil-in-water mixture.

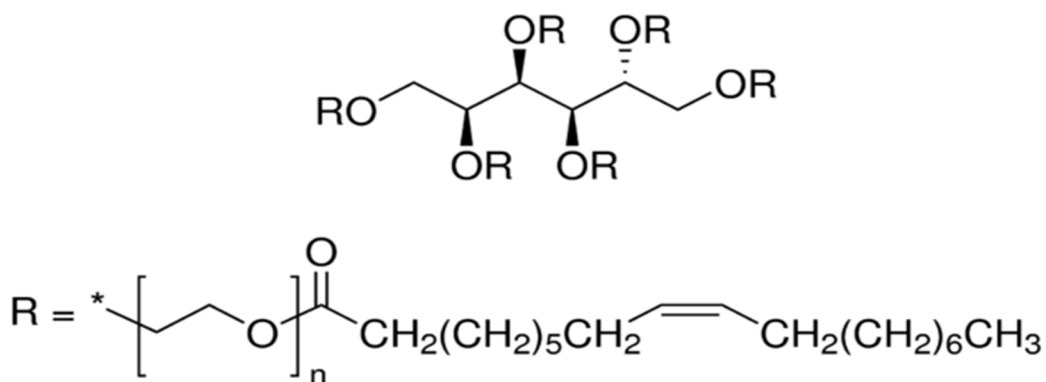


**Figure 1.** Polyethoxyethylene (POE) sorbitol hexaoleate (Atlas G-1086), the commonly used emulsifier in our WMO samples. The specific emulsifier in our sample had POE chains of length  $n = 40$ .

There is little published information regarding the long-term stability and curing of WMOs compared to their traditional counterparts, except for brief manufacturer materials,<sup>23</sup> providing a need in the paint and conservation communities for more information. It is expected that adding an emulsifying agent to paint could affect oxidative cross-linking processes, thus altering the molecular network of the WMO film.<sup>23</sup> It is important for conservation purposes to establish the curing and oxidative trends of these paint alternatives in order to determine the long-term viability of WMOs as an alternative to TOs.

The effects of treatments and other chemical processes on paint samples, including the addition of emulsifying agents to paint, can be investigated via single-sided NMR. A larger  $T_{2,\text{eff}}$  value indicates a less plastic molecular paint layer that potentially contains greater levels of free isotropic motion.<sup>22</sup> The assessment of the water mixable oil paints (WMOs) and the traditional oil paints (TOs) via single-sided NMR, supplemented with gas-chromatography mass spectrometry (GCMS) data, is presented in this thesis. The intent of the research is to assess the effects of the emulsifying agent on the molecular cross-linking and paint network formation of the oil paint.

## **Chapter 2: Background**

The background portion of this thesis will be broken down into two clear sections: (1) a detailed background on NMR theory used in our lab and (2) the background on the composition and chemistry surrounding the oil paints analyzed in this research.

### **NMR Theory:**

To provide a fundamental understanding of single-sided NMR, the physical concepts behind traditional NMR spectroscopy must be established. Therefore, this background will consist of an explanation of traditional NMR theory, to serve as preceding and comparison information for the background on single-sided NMR.

### ***Vector Model of Bulk Magnetization***

The properties of NMR spectroscopy rely on the fact that certain nuclei of interest, primarily  $^1\text{H}$ , possess both nuclear spin and angular momentum.<sup>24</sup> It is important to note that while  $^1\text{H}$  nuclei (protons) are primarily studied in NMR spectroscopy and our studies, other nuclei, including  $^{13}\text{C}$ ,  $^{19}\text{F}$ , and  $^{129}\text{Xe}$  also possess spin angular momentum, and as such are also NMR active. However, we exclusively utilize  $^1\text{H}$  NMR in our research. Associated with the angular momentum of each individual nucleus is a nuclear spin magnetic moment, in which the individual nucleus generates a small magnetic field. When this nucleus is placed in a magnetic field, an interaction between the nuclear magnetic moment and the extrinsic applied magnetic field ( $B_0$ ) occurs. The energy of this interaction depends on the orientation of the magnetic moment with respect to the magnetic field. When the two components are

oriented in a parallel fashion, or the angle between the two is zero, the interaction is at its lowest energy. Because the energy is lowest when spins are aligned, we get an overall alignment. The energy of spins in a sample are minimized if all of the individual magnetic moments of a nuclei in a sample are oriented parallel to the  $B_0$ , however this alignment is made difficult due to the thermal motion of molecules causing random spin orientations. To achieve the energetically favorable alignment of magnetic moments, the magnetic moments are aligned in such a way that the bulk magnetization of the sample, summed over all the spins, is parallel to the magnetic field. However, this is alignment is not as simple as it may seem. In a magnetic field, all nuclear spins can either align parallel or anti-parallel to the magnetic field. While the sum of all the spins equals a bulk magnetization vector that is parallel, most of the nuclear spins are cancelling each other out. A simple way of visualizing this phenomenon is as follows. Assume there are 20,000 nuclei in an isolated magnetic field. While 9999 of the nuclei in the system may spin anti-parallel to the magnetic field, 10,001 are spinning parallel to the field. When summing these spins, the net bulk magnetization would be parallel to the field due to the two spins that were not cancelled by an anti-parallel spin. The relative population difference of the spin states, known as polarization ( $p$ ), can be described by the following equation:

$$p = \frac{n_\alpha - n_\beta}{n_\alpha + n_\beta} \approx \frac{\Delta E}{2k_B T}$$



where  $n_\alpha$  is the population of the parallel (spin = +1/2) state,  $n_\beta$  is the population of the anti-parallel (spin = -1/2) state,  $\Delta E$  is the difference in energy between the two states,  $k_B$  is Boltzmann's constant, and  $T$  is temperature.

To better understand and visualize this bulk magnetization, we utilize a 3D vector model in which the equilibrium magnetization is a vector aligned with the z-axis. The axis system employed in the vector model is referred to as a right-handed axis, as illustrated in Figure 2. In the absence of an applied magnetic field, the magnetic moments are all randomly oriented, yielding a net zero magnetization. When a magnetic field is applied, the energetic preference for the moments to align parallel with the field allows the moments to adopt an energetically favorable alignment. This process by which the spins come to equilibrium in a magnetic field is known as relaxation.

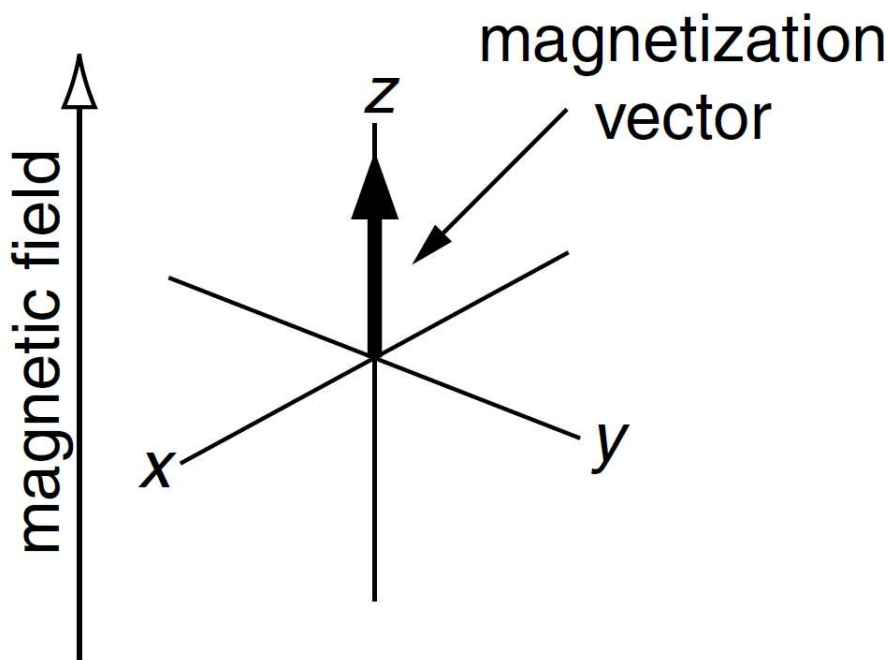


**Figure 2.** The right-hand magnetization vector used in the understanding of NMR. The bulk magnetization from the applied magnetic field  $B_0$  is located in the positive z-axis in the right-hand magnetization vector. From [23]

### *Nuclear Precession*

The formation of an equilibrium magnetization vector aligned with the z-axis entails that the equilibrium magnetization is constant in both size and direction. When an applied pulse, which will be later discussed, interacts with the equilibrium magnetization, the vector is tipped away from the z-axis. The magnetization vector then begins to rotate in a conical shape about the z-axis, as shown in Figure 3, through a phenomenon known as precession. The frequency ( $\omega_0$ ) of this precession about the field, also known as the Larmor frequency, is described via the equation:

$$\omega_0 = -\gamma B_0$$

where  $\gamma$  is the gyromagnetic ratio, a constant unique to each nucleus. In a pulsed NMR experiment, the Larmor precession is what is always detected. To do so, a coil of wire is placed around the sample with the axis of the coil aligned in the xy-plane. As the precessing magnetization interacts with the coil, an induced current is produced. This current is then amplified and recorded. The signal produced from this current is known as the free induction signal, or more commonly, the free induction decay (FID).<sup>25</sup>

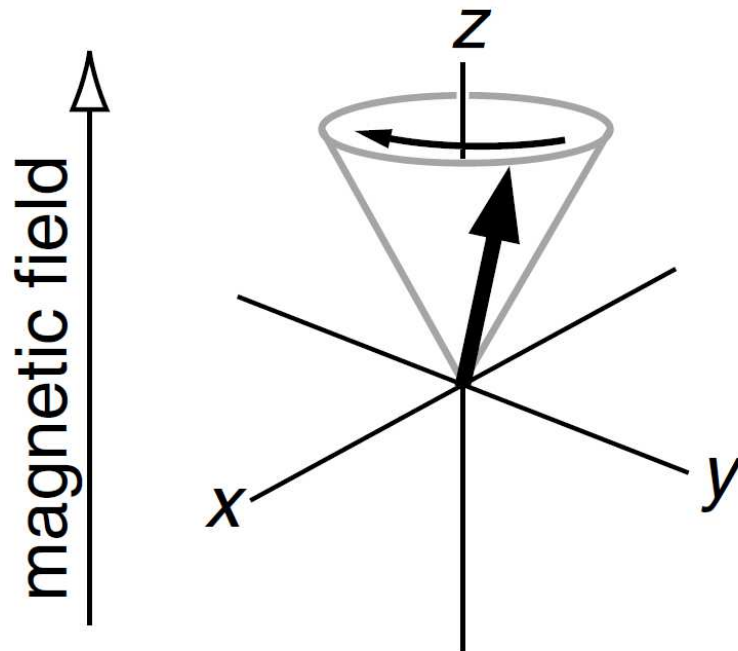


**Figure 3.** The bulk magnetization vector under only the applied magnetic field ( $B_0$ ) is located parallel to the magnetic field along the z-axis (see figure 2). When the magnetization vector receives energy from an outside power, it is able to tilt away from the z-axis. This tilting causes the magnetization vector to begin precession about the z-axis in a conical shape, as depicted. From [23]

## *Pulses*

To rotate the magnetization away from the z-axis, and begin Larmor precession, resonance must be utilized. Through use of the same coil used to detect the Larmor frequency, a radiofrequency (RF) pulse is applied to the system perpendicular to the equilibrium magnetization, as displayed in Figure 4. It is imperative that this new applied field oscillates at or near the Larmor frequency, allowing for the oscillating field to become resonant with the Larmor precession frequency. By utilizing resonance, the oscillating magnetic field can shift the bulk magnetization into the xy-plane, overcoming the substantially larger  $B_0$  magnetic field from the magnet. This common case in regards to dealing with the RF pulses is known as an on-resonance pulse. In an on-resonance pulse, the Larmor precession frequency offset ( $\Omega$ ) is zero, allowing the effective field to lie along the x-axis of the vector plane. The tilt angle ( $\theta$ ) of the effective field is thus  $\pi/2$  or  $90^\circ$ , assuming proper calibration of the pulse length, and as such we refer to an on-resonance excitation pulse as a  $\pi/2$  or  $90^\circ$  pulse.

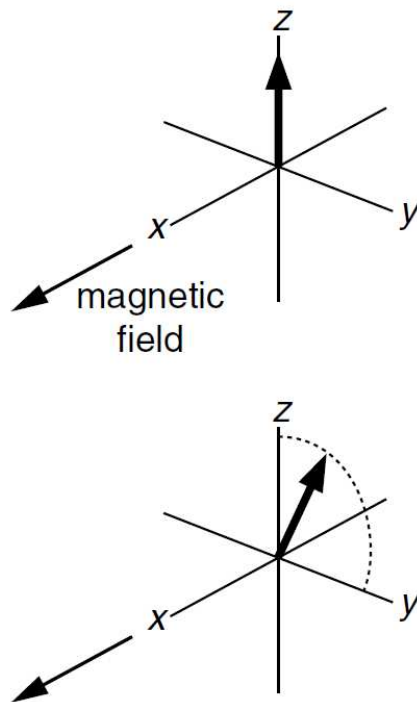


**Figure 4.** As the RF coil produces a  $90^\circ$  or  $\pi/2$  pulse, the magnetic field along the z-axis is shifted quickly onto the x-axis, as shows by the arrow. This shift causes the bulk magnetization vector to fall into the transverse xy-plane, where it continues its precession. From [23]

The use of on-resonance pulses allows for the most basic example of an NMR experiment to occur: the pulse-acquire experiment. In a simple pulse-acquire experiment, diagrammed in Figure 5, there is a three-period mechanism. In period 1, equilibrium magnetization is allowed to build up along the z-axis. Period 2 entails the use of a  $90^\circ$  ( $x$ ) pulse to rotate the magnetization onto the  $-y$ -axis. Finally, period 3 entails acquiring the signal of the precession in the transverse  $xy$ -plane.

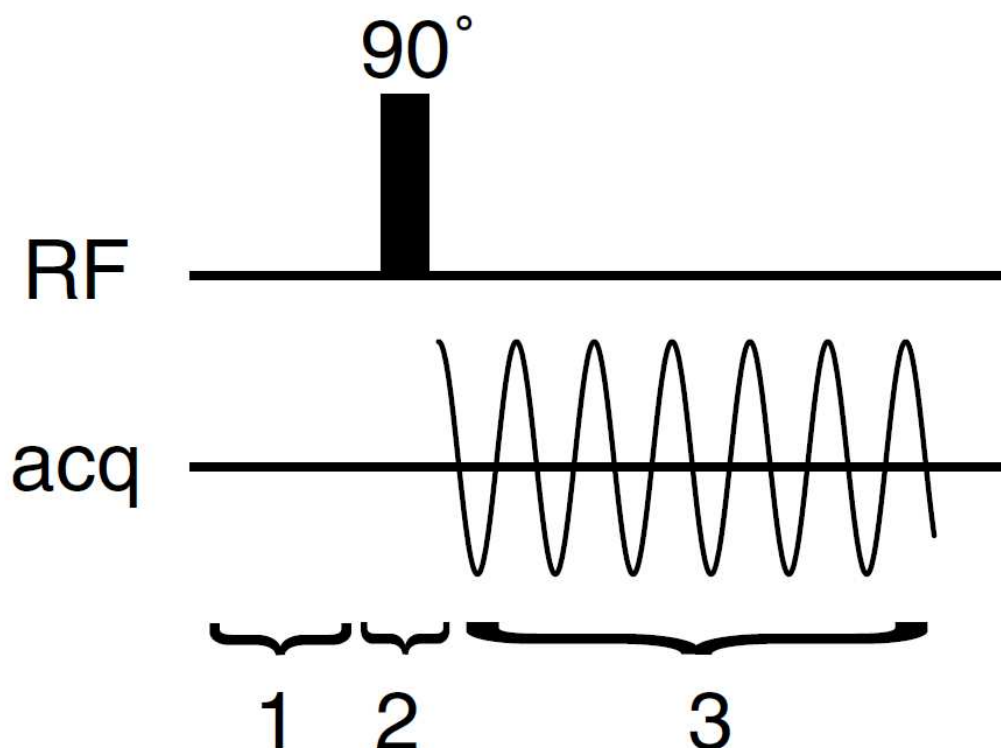


**Figure 5.** A simplified diagram of the basic pulse-acquisition experiment. The “RF” line shows the location of the radiofrequency pulses, whereas the line marked “acq” shows when the signal recorded or acquired. In step 1, the bulk magnetization vector is allowed to reach equilibrium under the influence of the applied magnetic field. Step 2 entails application of the  $\pi/2$  on-resonance excitation pulse required to move the magnetization into the  $xy$ -plane. Step 3 diagrams the precession in the transverse plane as a FID; during this time the precessional frequency is acquired. From [23]

## Single-Sided NMR

### *Instrumentation and Limitations*

The single-sided NMR field was revolutionized with the invention of the NMR-MOUSE (**MO**bile **U**niversal **S**urface **E**xplorer - Magritek), the very same instrument utilized in our own lab. The NMR MOUSE, whose magnetic field is depicted in Figure 6, involves applying “inside-out” NMR, a form of NMR in which the sample is external to the apparatus, but is still similarly probed by radiofrequency (RF) fields.<sup>26</sup> In the NMR MOUSE apparatus, the static magnetic field is generated by permanent magnets with anti-parallel magnetization. A solenoidal RF coil is then positioned between the permanent magnets, allowing for the polarizing magnetic field ( $B_0$ ) and the applied RF field ( $B_1$ ) to be orthogonal to each other. This setup allows for a reasonably large volume above the magnet in which  $B_0$  and  $B_1$  are orthogonal to one another, providing a spatial resolution on the order tens of microns in the Z plane and centimeters in the X-Y plane.

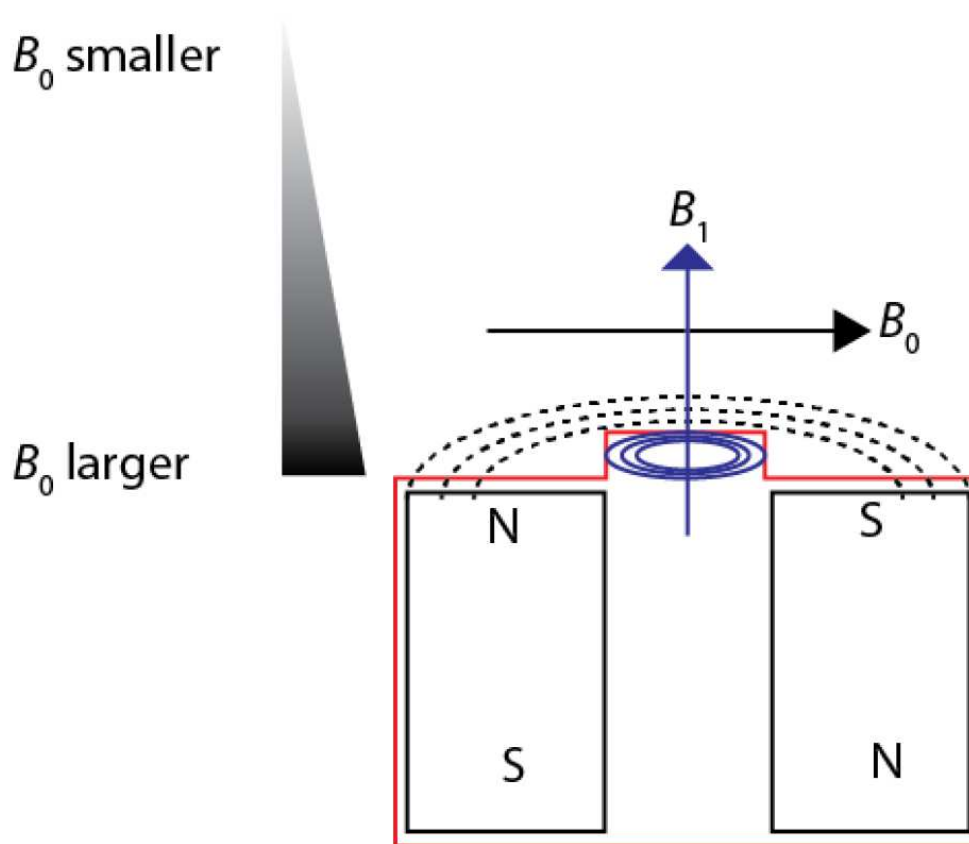


**Figure 6.** A cross-sectional representation of the NMR-MOUSE single-sided apparatus. The presence of the N-S block magnets produces an applied magnetic field ( $B_0$ ) in which the strength of the field diminishes as distance away from the magnet housing is increased. The blue rings depict the presence of the RF-coil and corresponds to the RF magnetic field also depicted in blue. The RF magnetic field ( $B_1$ ) is responsible for moving the magnetic field away from the applied magnetic field, and allows for Larmor precession in the xy-plane.



The NMR-MOUSE apparatus uses permanent block magnets incapable of producing a homogeneous magnetic field. As a result, the nuclei in the magnetic field each experience a different force. Furthermore, single-sided NMR apparatuses incorporate a strong field gradient, making specific observations in high-field or traditional NMR, such as chemical shifts, significantly more difficult to measure with single-sided NMR. To compound the issues surrounding the field inhomogeneity of the single-sided magnets, there are also issues that require a modification to the pulse sequence used in traditional NMR pulse-acquire experiments. With our instrument, we are unable to apply an on-resonance pulse and instantly acquire precession data due to a much greater contribution from the “dead time.” During the “dead time” immediately following the excitation, the RF coil still has residual energy which has yet to leave the coil. The RF coil, used for both the excitation and detection, cannot have residual energy in the coil at the time of detection. If acquisition were to occur with energy still in the coil, the receiver of the MOUSE would essentially be given too much power and malfunction. The “dead time” is thus required in order to allow the extra energy in the RF coil to first dissipate, but this in turn leaves the spectrometer without enough time to measure the signal from the Larmor precession via FID before the signal has decayed due to a loss of coherence among spins.

To overcome this limitation in the design of the MOUSE magnet, the utilization of Hahn echoes<sup>27</sup> and the CPMG sequence<sup>21</sup> is required. Hahn echoes, detailed in Figure 7, involve acquiring an echo of the original signal through use of a  $180^\circ$  or  $\pi$  pulse that we refer to as a refocusing pulse. The refocusing pulse is responsible for inverting the bulk magnetization vector within the xy-plane. To clarify, each individual nucleus in an

inhomogeneous magnetic field carries a specific magnetic moment that experiences different force from the applied magnetic field. Due to the inhomogeneous field, these magnetic moments precess at different frequencies. After a period of time, the various frequencies of precession from individual magnetic moments lead to a total decay of the FID signal, at which point the refocusing pulse is applied. Upon the application of the refocusing pulse, the individual magnetic moments return to their respective orientations in the xy-plane after a time equivalent to that between the excitation and refocusing pulses as diagrammed in Figure 8. By timing the time between each pulse ( $\tau$ ) to be greater than that of the “dead time” of the RF coil and receiver, the echo of the FID can be recorded without any obstruction. By performing the Hahn echo, the FID signal amplitude can be recorded. However, chemical shift data is lost when implementing the Hahn echo. To improve upon the Hahn echo, the CPMG pulse sequence was created.

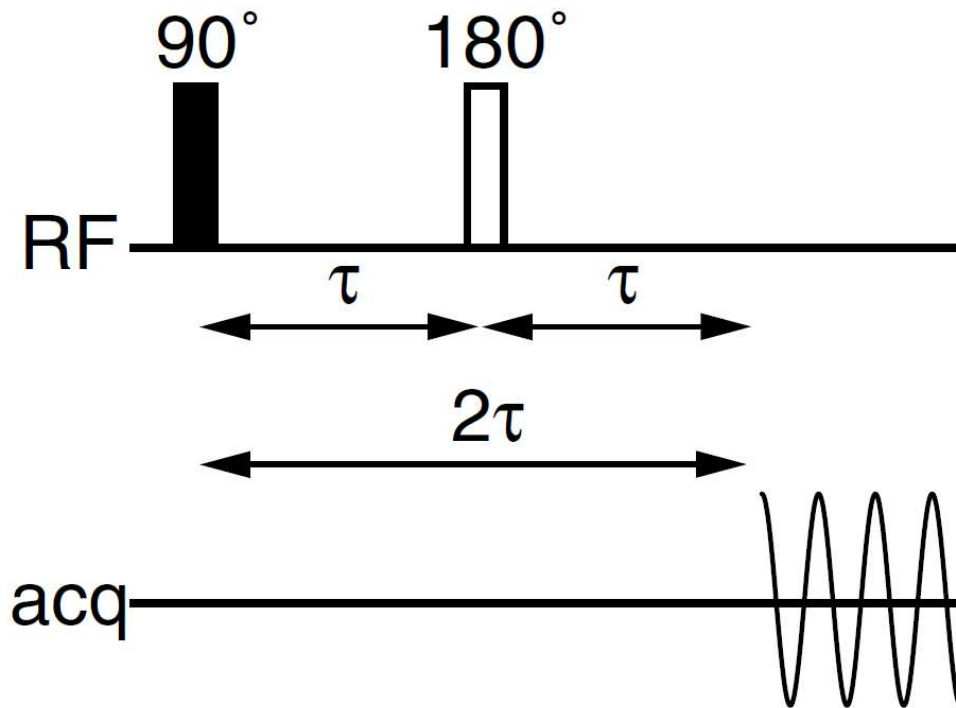


**Figure 7.** Diagram of the Hahn echo utilizing the same format as Figure 5. In order to overcome complications associated with the dead time due to residual RF energy, a Hahn echo pulse sequence must be utilized. After the application of the on-resonance excitation  $\pi/2$  pulse, precession is allowed to occur for a set time,  $\tau$ . After that time, a  $\pi$  refocusing pulse is applied and an equal amount of time is allowed to pass before acquisition of the FID signal amplitude. From [23]

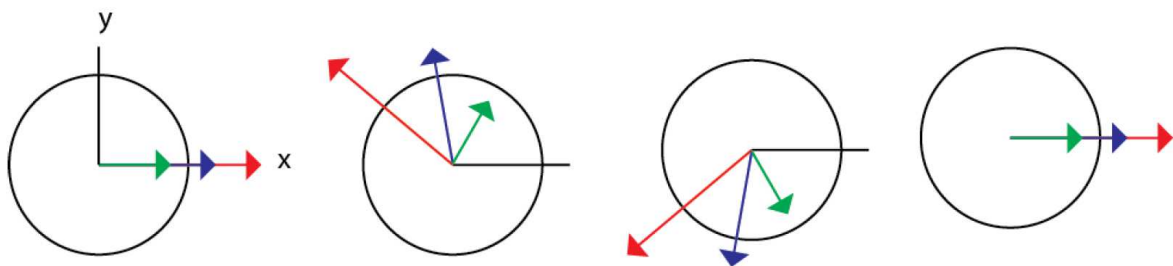


**Figure 8.** A depiction of the refocusing of individual magnetic moments through a refocusing pulse. As discussed in the text, due to field inhomogeneity, the individual nuclei each precess with a slightly different frequency. As these individual magnetic moments precess under different field strengths (indicated by the length of the arrow drawn), dephasing begins to occur, as diagrammed in the second circular image. A refocusing pulse can then be applied to invert the magnetic moments about the x-axis, and the magnetic moments can converge once again on the x-axis. This provides an opportunity to thus measure the echo of the FID.

The CPMG pulse sequence shown in Figure 9 involves a specific number of repetitions of the Hahn echo, in which the  $180^\circ$  refocusing pulse is applied multiple times while alternating its phasing with respect to the initial  $90^\circ$  on-resonance pulse, providing multiple echoes corresponding to the amount of refocusing pulses used. These iterations of echoes decay in signal over time due to relaxation.

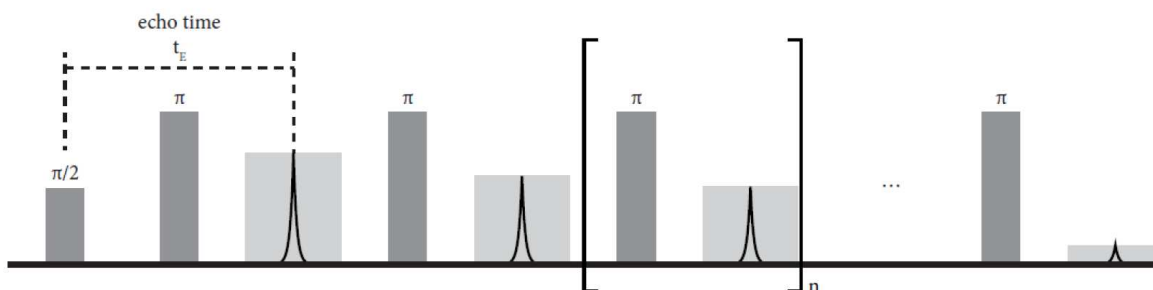


**Figure 9.** A simplified diagram of the CPMG pulse sequence, consisting of numerous iterations of Hahn pulses. An initial on-resonance excitation pulse followed by a refocusing pulse allows for the acquisition of a single Hahn echo. Once precession has occurred for half of the echo time ( $t_E$ ), another refocusing pulse can be applied and eventually another echo is recorded. This process is repeated  $n$  number of times, as determined by the user. As diagrammed in the figure, after each refocusing pulse the amplitude of the FID signal decreases, creating an echo train that we fit with a mono-exponential decay curve. From this curve, we can determine the transverse relaxation time of the sample.

## Relaxation

Relaxation is the process by which the bulk magnetization of a system reaches decoherence or equilibrium, depending on the type of relaxation. The first and more important form of relaxation for this research is  $T_2$  or transverse relaxation. Transverse relaxation is the phenomena by which the transverse magnetization decays towards a net value of zero; thus, having reached decoherence. As the individual magnetic moments in the inhomogeneous magnetic field precess at different frequencies, the frequencies begins to diphas from one another. Eventually, the vector components of the individual magnetization cancel each other out, resulting in the total decay or decoherence of the FID signal amplitude at a specific time. This rate of decoherence is described by  $T_2$ , the transverse relaxation time. The use of CPMG experiments allows for NMR methods to measure the transverse relaxation time.  $T_2$  relaxation is considered to follow first order kinetics, resulting in a simple exponential decay characterized by the following equation:

$$\frac{S}{S_0} = e^{-t/T_2} \text{ or } \ln\left(\frac{S}{S_0}\right) = \left(\frac{-1}{T_2}\right)t$$

Where  $S$  is the measured signal intensity,  $S_0$  is the greatest signal intensity measured overall, and  $t$  is the time after excitation. By utilizing  $S_0$  to normalize the signal and taking the natural logarithm of both sides of the equation, a plot of the intensity of the signal vs. time can be generated to determine the transverse relaxation value. It is important to note that the use of the CPMG with our magnets actually measures a value known as the effective transverse relaxation, or  $T_{2,\text{eff}}$ . While  $T_2$  is simply a measure of the decoherence of the FID within one echo,  $T_{2,\text{eff}}$  correlates to the loss in total FID signal over a sum of echoes. While  $T_2$  directly measures the material,  $T_{2,\text{eff}}$  is a measure

of the material with experimental parameters. If there were a scenario in which the echo time for an experiment was 0, the  $T_{2,\text{eff}}$  would equal  $T_2$ . For the purposes of this thesis,  $T_{2,\text{eff}}$  will be referred to as  $T_2$ .

Another important form of relaxation not measured or used in this research is  $T_1$  or spin-lattice relaxation. Spin-lattice relaxation is a direct measure of the length of time required for the magnetization in the transverse plane to return to thermodynamic equilibrium. Like transverse relaxation, spin-lattice relaxation also follows an exponential decay. The textbook on single-sided NMR by Blümich et al. is a good resource for material regarding spin-lattice relaxation and single-sided or low-field NMR instruments.<sup>28</sup> By using relaxation values, certain physical properties and processes of materials can be elucidated. This is the primary focus of the NMR experiments used to analyze oil paint samples.

## Oil Paints

### *Oil Paint Composition*

Traditional oil paints (TOs) are a form of slow-drying paint that consist of a homogenous mixture of pigment particles suspended in a drying oil or binder – commonly linseed oil from flax plants or sunflower seed oil. TOs need an oil that hardens into a solid paint film, typically requiring a high concentration of polyunsaturated fatty acids to undergo the process of auto-oxidation for curing. The principle components of linseed and sunflower oils used as the base for the oil paints are triglycerides composed of glycerol and fatty acids.<sup>29</sup> The unsaturated fatty acids are

primarily oleic (C18:1), linoleic (C18:2), and linolenic (C18:3). Furthermore, several other saturated fatty acids, including azelaic acid (a C9 dicarboxylic acid), stearic acid (C18:0), and palmitic acid (C16:0), are also found in the seed oil composition. The other common component in TOs, besides pigments made of minerals, organisms, and “earth” components, are metal oxides such as zinc, aluminum, and copper which can operate as stearates or catalysts within the paint network. These oxides are commonly used as both pigment additives in order to produce more vibrant colors, and also as metal centers used to catalyze autoxidation in paint films and stabilize the paint film network.<sup>30</sup> Aluminum and zinc stearates in many instances are added as driers and paint stabilizers, pigment dispersants, and gelling agents.<sup>31</sup> Some paintings exhibit brittleness, cracking, lumps, or delamination of paint layers from migration of metal soaps or zinc oxide underlayers.<sup>32</sup>

While standard drying oils, such as linseed oil, are typically used in oil paint creation, some non-drying oils or semi-drying oils are also used, potentially for their ability to produce more vivid or long-lasting color. Certain paintings testing positive for the presence of sunflower, safflower, and castor oil, which are semi-drying or non-drying oils, have had issues concerning the liquid structure and lack of dryness in the sample paint network.<sup>33,34</sup> Furthermore, studies of paintings created with TOs in the 1960's have been shown to exhibit surface wrinkling where castor and rapeseed oils were identified. The presence of semi and non-drying oils in large enough quantities can impede the paint film drying process, creating future preservation issues. In addition to the variety of surface issues, many oil paintings have been found to be sensitive to the use of aqueous and organic solvents. Several dry materials, emulsions, and gels have



been proposed to off-set the effects of using pure solvents to clean these sensitive paintings and testing for effective and safe methods for cleaning and storage continues today.

As mentioned, the additive in the WMOs that gives them their water-miscibility is an emulsifying agent; in the Grumbacher Max paint samples (WMOs), it is called Atlas G-1086. Atlas is a polyoxyethylene (POE) sorbitol hexaoleate derivative consisting of six long, unsaturated fatty acid chains with centers of  $n = 40$  POE insertions. The emulsifying agent component allows for binding into the triglyceride paint film network. This combination allows for a cured paint film to form under the same conditions of TO paint curing.

Both TO and WMO samples contain numerous different fatty acids that reflect the initial composition of the paint as well as the overall curing progress of the paint layer. Because curing processes affect the relative amounts of these fatty acids in a paint film, analysis of fatty acid content can illuminate the drying potential and curing progress of a paint sample.<sup>35,36</sup> Fatty acid concentrations are not directly determined, but instead are calculated via GCMS in terms of ratios between fatty acids.<sup>37</sup> The primary fatty acids of importance are azelaic (A), palmitic (P), steric (S) and oleic acid (O). These acids ratios can be used to track certain properties of paint films.

### *Oil Paint Curing: Auto-Oxidation*

Curing of oil paints proceeds via two steps: (1) a physical drying step in which the volatile compounds in the paint evaporate and (2) an autoxidative step where chemically cross-linked oligomers form the basis of a matrix that both holds the paint

together and forms a rigid and dry paint film (Figure 10).<sup>30,31,38</sup> The process of autoxidation occurs through a free-radical chain mechanism characterized by initiation, propagation, and termination steps (Figure 11). In the first part of the initiation step, atmospheric oxygen reacts with fatty acid chains at points of unsaturation, removing the carbon-carbon double bond to produce a hydroperoxide. Because the initiation step relies on resonance stabilization, monounsaturated oleic acids typically go through the autoxidation process slower, as a result of their lack of diene character. For this reason, a higher concentration of oleic acid indicates a paint film that is less cured. Following the first step of initiation, the second step entails the hydroperoxide decomposing into both peroxy radicals ( $\text{ROO}^{\bullet}$ ) and oxygen radicals ( $\text{RO}^{\bullet}$ ). During the propagation step, the oxygen radicals produced from the decomposition of hydroperoxide abstract hydrogen from nearby carbons to produce allylic radicals and alcohols ( $\text{ROH}$ ), and the peroxy radicals abstract hydrogen to produce more hydroperoxide, which in turn feeds back into the initiation step, increasing autoxidation. In the termination step, the allylic radicals, as well as the peroxy and oxygen radicals from the hydroperoxide decomposition, form cross-linkages. Peroxy cross-links ( $\text{ROOR}$ ) and ether cross-links ( $\text{ROR}$ ) are most common, but C-C cross-linkages ( $\text{R-R}$ ) also occur. This cross-linking forms the rigid structure of the cured paint films. Figures 10 and 11 demonstrate both the reaction pathway for auto-oxidation, as well as one of the various potential cross-linkages that can occur.<sup>30</sup> If another outside molecule, such as an emulsifier, were capable of cross-linking into the paint film, it could provide greater molecular mobility by

altering both intramolecular and intermolecular cross-linking among adjacent fatty acid chains through insertion of large non-reacting molecules.

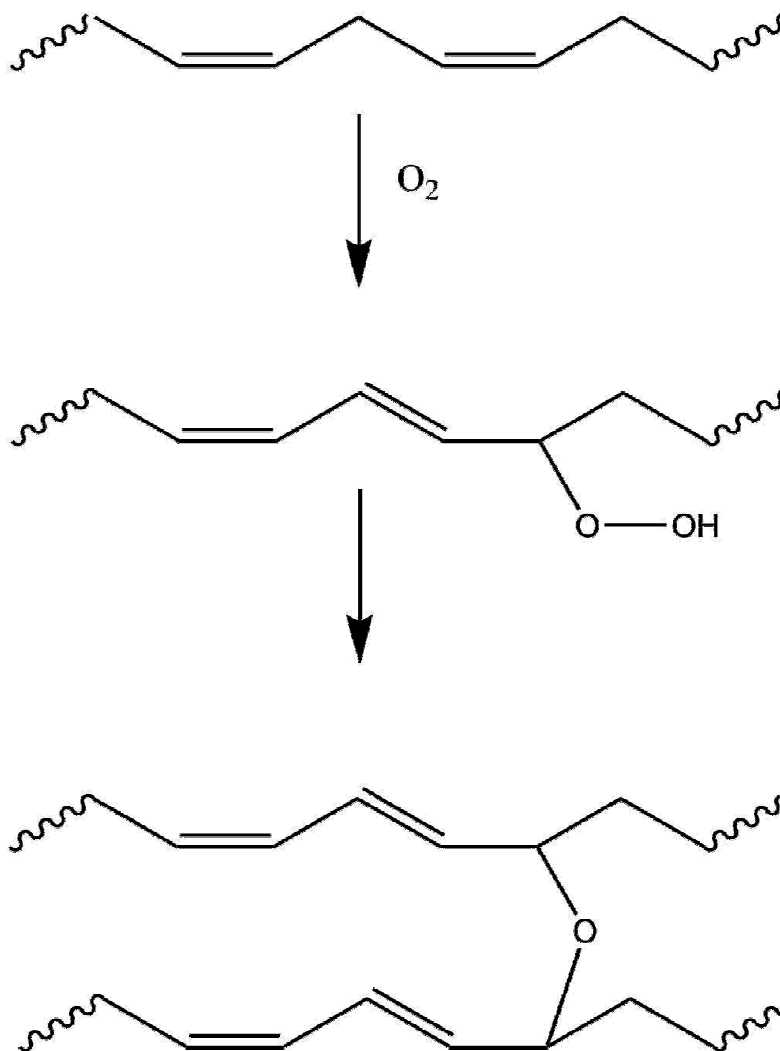


**Figure 10.** A depiction of the cross-linking formed between adjacent glyceride chains in the paint film. The formation of these chains produces a more stable paint film as it dries, as well as a more molecularly rigid paint network.

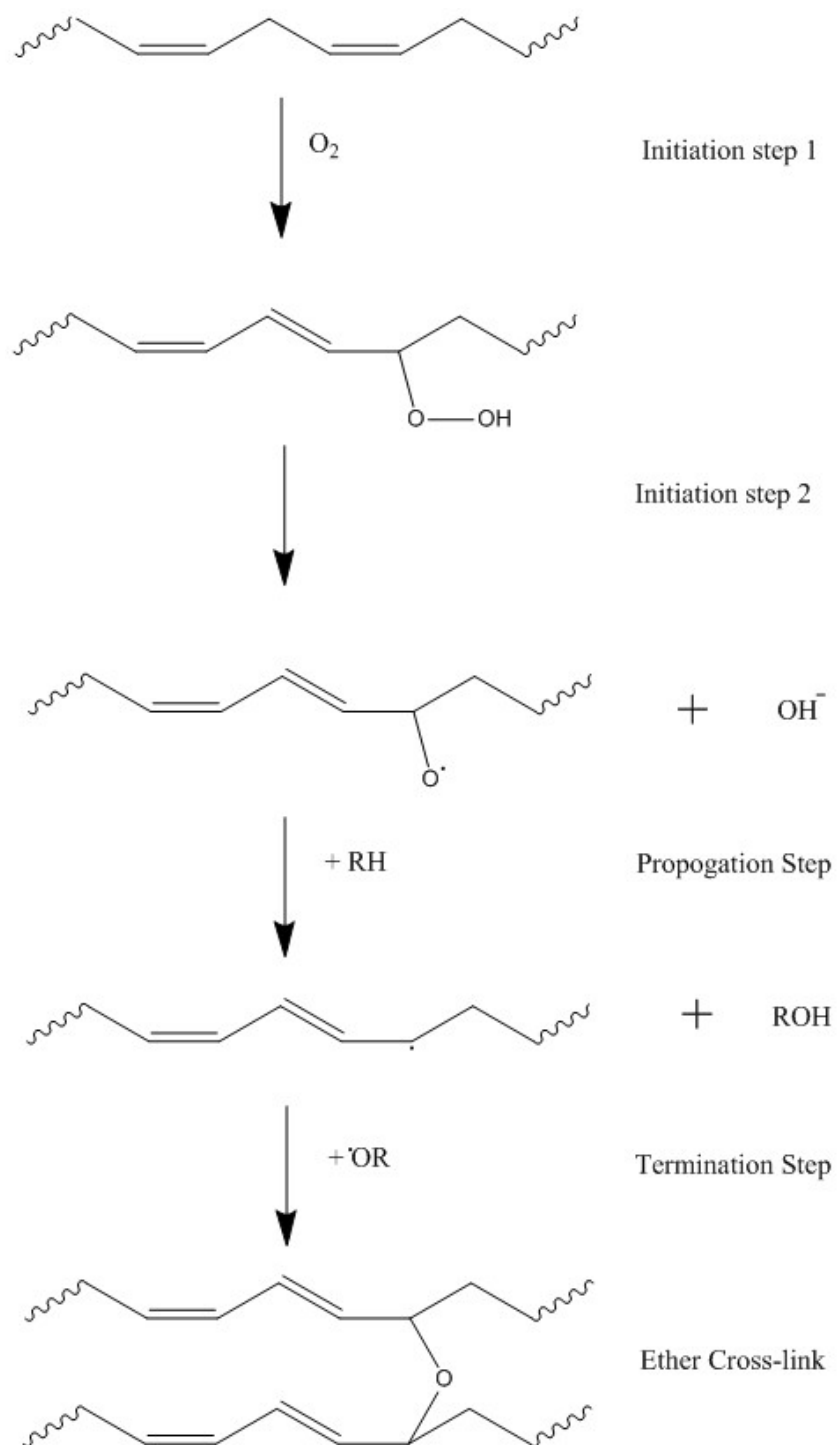


**Figure 11.** One of the mechanisms responsible for producing cross-linkages in the paint film network. While this figure shows a mechanism for the formation of an ether cross-link, there are other potentially cross-linkages possible, including peroxy cross links and carbon-carbon cross-links. Adapted from [30].

### *Oil Paint Curing: $\beta$ -Scission*

The other main curing process competing with autoxidation is  $\beta$ -scission, a chemical process by which radicals formed during the propagation step of autoxidation lead to an oxidative cleavage of the fatty acid chains on the bond adjacent to a point of unsaturation. From there, the separate components can form dicarboxylic acids and various alcohols via oxidative reactions. These dicarboxylic acids and alcohol derivatives are unable to interact with the fatty acid networks, thus reducing cross-linking. An example of a common  $\beta$ -scission product is azelaic acid, formed from unsaturated fatty acids (Figure 12). Azelaic acid is a potential product of oleic, linoleic, and linolenic acids, and because it is formed as a product of  $\beta$ -scission, the presence of azelaic acid can be measured as an indicator to determine paint curing. The most common means of monitoring the presence of azelaic acid is by monitoring a ratio between azelaic acid and palmitic acid (A/P ratio).<sup>37</sup> As it is fully saturated, the concentration of palmitic acid does not change significantly over time. A greater concentration of azelaic acid is indicative that the primary fatty acid chains in the paint film have undergone  $\beta$ -scission reactions, and by extension the paint film has undergone greater levels of curing.

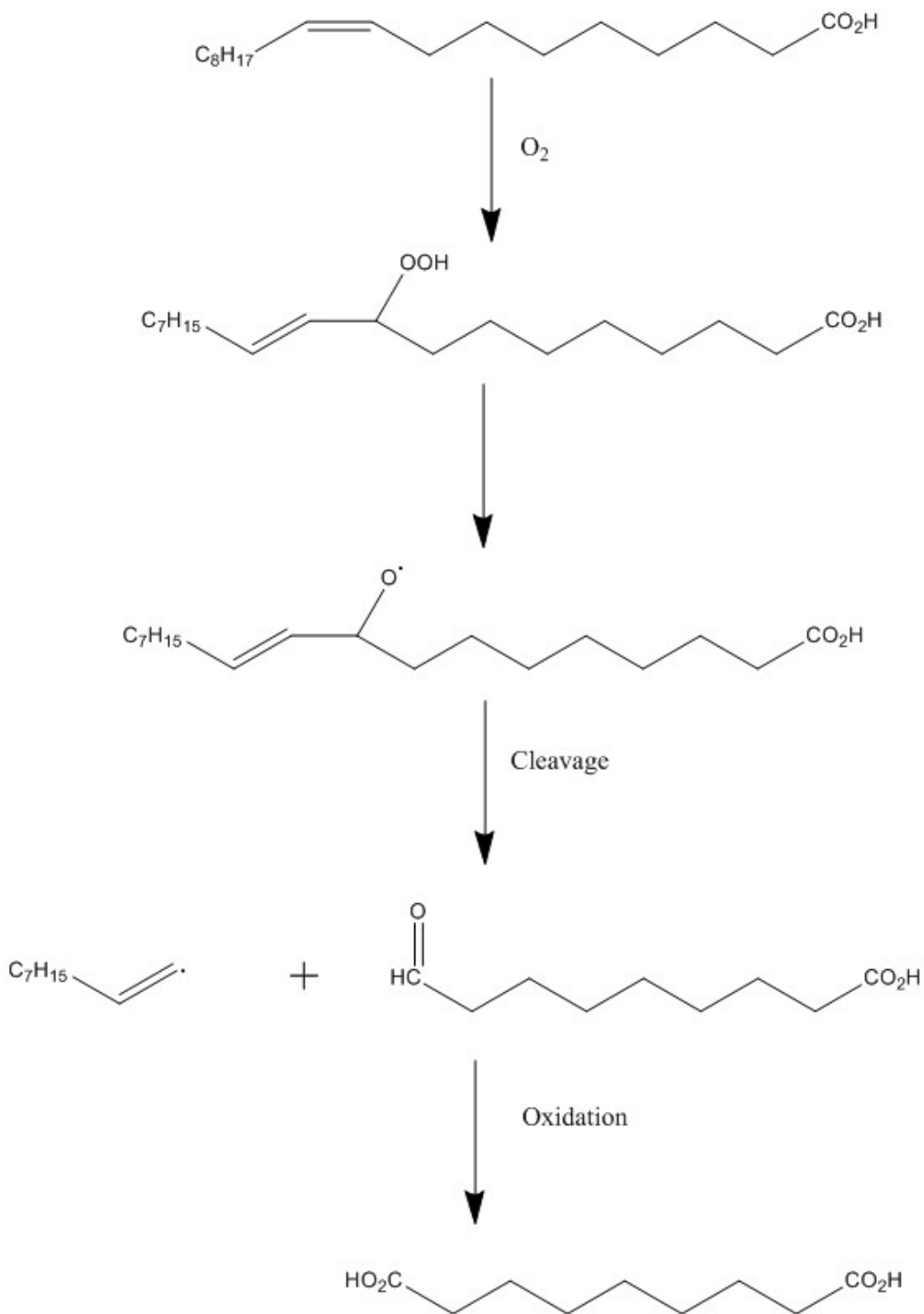


**Figure 12.** A simplified mechanism for the formation of azelaic acid from oleic acid via  $\beta$ -scission. Cleavage of the carbon-carbon bond adjacent to the point of unsaturation and the alkoxy radical produces the intermediate of azelaic acid as shown. From there, slow oxidative mechanisms produce azelaic acid.

### **Chapter 3: Experimental**

#### **Paint Samples:**

The samples measured include the traditional (TO) and water-mixable (WMO) oil paints (Grumbacher, Pre-tested Professional and Max series, respectively) in the following colors: alizarin crimson (pigment 001), cadmium red light (027), diarylide yellow (060), Grumbacher red (095), thalo green (205), soft titanium white (212), viridian (232), and titanium white (250, TO only). NMR values for the various pigments were of approximately the same order; therefore, data recorded from the various pigments of paint were treated in aggregate, instead of focusing on individual pigments. Three different sample sets were aged for different times, providing data on curing. These samples were produced in 1995, 2014, and 2015. Figure 13 provides reference images of the individual paint and emulsifier samples.

#### ***Sample Group A: 1995 paintouts***

Naturally aged reference samples came from the National Gallery of Art's (NGA) Artists' Materials Study Collection. In 1995, the Grumbacher Factory in New Jersey created comparison paintouts of WMOs and TOs on canvas and boards prepared with two types of grounds: a traditional oil ground and an acrylic ground. These paintouts were acquired by the NGA Conservation Division between 2003 and 2005. They provide the possibility for direct comparison between WMOs and TOs that have been stored and aged under the same conditions for 20 years. Only the paintouts on an acrylic ground on canvas were used in this study. The paintouts were 260 months old at the time their properties were measured. Furthermore, these samples measured

roughly 45 cm high by 60 cm wide with each individual paintout (seven per board or canvas) being 12 cm high by 4.5 cm wide; making the paint areas well beyond large enough to cover the entire sensing region of the magnet. Each individual layer of paint was roughly 125  $\mu\text{m}$  thick prior to curing.

#### *Sample Group B: 2014 paintouts*

Tubes of TOs and WMOs were purchased in January of 2014. Most the paint tubes contain copyright dates ranging from 2011 to 2013 with a few exceptions as early as 2000. Sample Group B was produced by applying each individual paint onto a 2 cm high by 8 cm long borosilicate glass slide (1 mm thick) using a 4 mil (101.6  $\mu\text{m}$ ) drawdown bar. These samples were produced in early 2014 and were analyzed after approximately 30 months of curing using both GCMS and single-sided NMR.

#### *Sample Group C: 2015 paintouts*

The same paint tubes used to produce Sample Group B were used to produce a similar set of slides in August 2015. These slides were produced by applying the paint to an equal dimension borosilicate glass microscope slide using a 100  $\mu\text{m}$  drawdown bar. Measurements were made in approximately 2 month increments over the period of a year.

#### *Sample Group D: Linseed oil and Atlas mixture samples*

Four samples were prepared to assess the effects of the emulsifier (Atlas G-1086) on the constitution of the alkali-refined linseed oil (ARLO), the primary oil



component in both traditional and water-mixable oil paints. Atlas G-1086 (Chem Service Inc.) consists of  $n = 40$  polyoxyethylene (POE) fragments in the POE sorbitol hexaoleate (see Figure 1). Three mixtures of Atlas G-1086 in ARLO were made with weight percentages of 5.7, 7.1, and 9.2. Each of these samples was poured onto 1 mm thick borosilicate glass microscope slides and dispersed using a paintbrush. A fourth glass slide was produced similarly but contained only ARLO for reference. NMR measurements were obtained when the samples had been curing for 18 months.

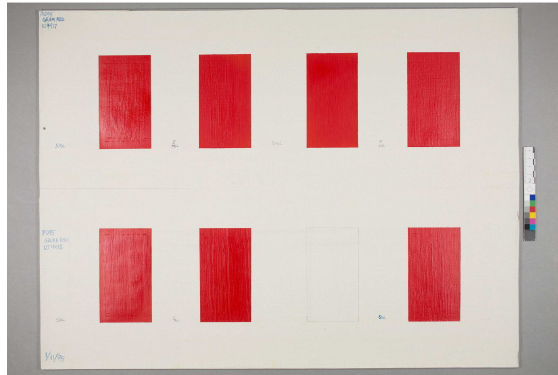


**Figure 13.** Images of the various types of samples analyzed during this research, including: Sample Group A Canvas sample (top), an assortment of Sample Group C paint samples (middle), and a Sample Group D sample (bottom).

## GCMS:

### *Reagents used for GCMS analysis*

Three common derivatization agents, TMTFTH, TMAH (25 wt%), and TMSH, were tested on castor wax at room temperature overnight. Temperature and reaction time conditions were tested on castor wax and Max Prussian blue samples to optimize completion of derivatization. Methanol (Optima, 0.2  $\mu\text{m}$  filtered, Fisher Scientific) was used to dilute reagents and samples as needed. Other details of the GCMS procedure are accessible through the National Gallery of Art and set to be published elsewhere.

### *GCMS Procedures*

TMAH was diluted from 25% to 2.4 wt% in methanol. Paint samples were pretreated with 40  $\mu\text{L}$  of the 2.4% TMAH-methanol solution and heated at 80  $^{\circ}\text{C}$  for 1 h. GCMS analysis was conducted using a Varian 3900 gas chromatograph with a Restek Rxi®-1301Sil MS (30 m, 0.25 mm ID, 0.25  $\mu\text{m}$ ) column coupled to a Varian Saturn 2100T ion trap mass spectrometer operating in EI mode (70 eV). The scan range was  $m/z$  42–650 except for 8–8.5 min when the range was narrowed to  $m/z$  44–158. Helium carrier gas was used in constant flow mode (1.1  $\text{mL min}^{-1}$ ). Samples were injected using a Varian CP8400 autosampler (1  $\mu\text{L}$ ). The GC inlet temperature was 300 $^{\circ}\text{C}$ . The GC oven temperature was programmed from 65 $^{\circ}\text{C}$  with a 2 min hold, increased at 14 $^{\circ}\text{C min}^{-1}$  to 230 $^{\circ}\text{C}$  with a 2.1 min hold, and then increased at 14 $^{\circ}\text{C min}^{-1}$  to 290 $^{\circ}\text{C}$  with a final 6.5 min hold; total run time 26.7 min. Data processing was done using Automated

MassSpectral Deconvolution and Identification System (AMDIS) 2.70 software from the National Institute of Standards and Technology, and Microsoft Excel.

### Single-Sided NMR

#### *Instrumentation*

All NMR experiments were performed using a PM-5 NMR-MOUSE (Magritek, New Zealand), with an applied field strength of approximately 0.4566 T (calculated 19.44 MHz proton frequency), connected to a Kea2 spectrometer (Magritek). The PM-5 name denotes that the magnet is accurately able to obtain signal from a sample up to 5 mm from the RF coil in the vertical direction. Furthermore, the spatial resolution of the NMR-MOUSE coil is approximately a 1-inch square area. The option to add or remove 2 mm thick spacers was available for all the various measurements, and was employed in some of the experiments. Figure 14 provides an image of the entire outline of the NMR-MOUSE layout and external design. While the magnets and RF coil provide the magnetic fields, all RF generation and pulse programming are controlled by a PC-based NMR console running the program Prospa (Magritek), attached to a spectrometer. The Kea spectrometer (Magritek) utilized in our research is lightweight and capable of operating at up to 400 MHz frequencies; well above the frequencies used in our lab. For all measurements, the magnet assembly was mounted to a custom lift (Magritek) that moved the magnet vertically with respect to the samples in order to localize the region of greatest signal. The larger samples from Sample Group A required stabilization over

the magnet via a handmade wooden platform. The platform contained no metal within distance of the magnet that would affect the NMR experiments.

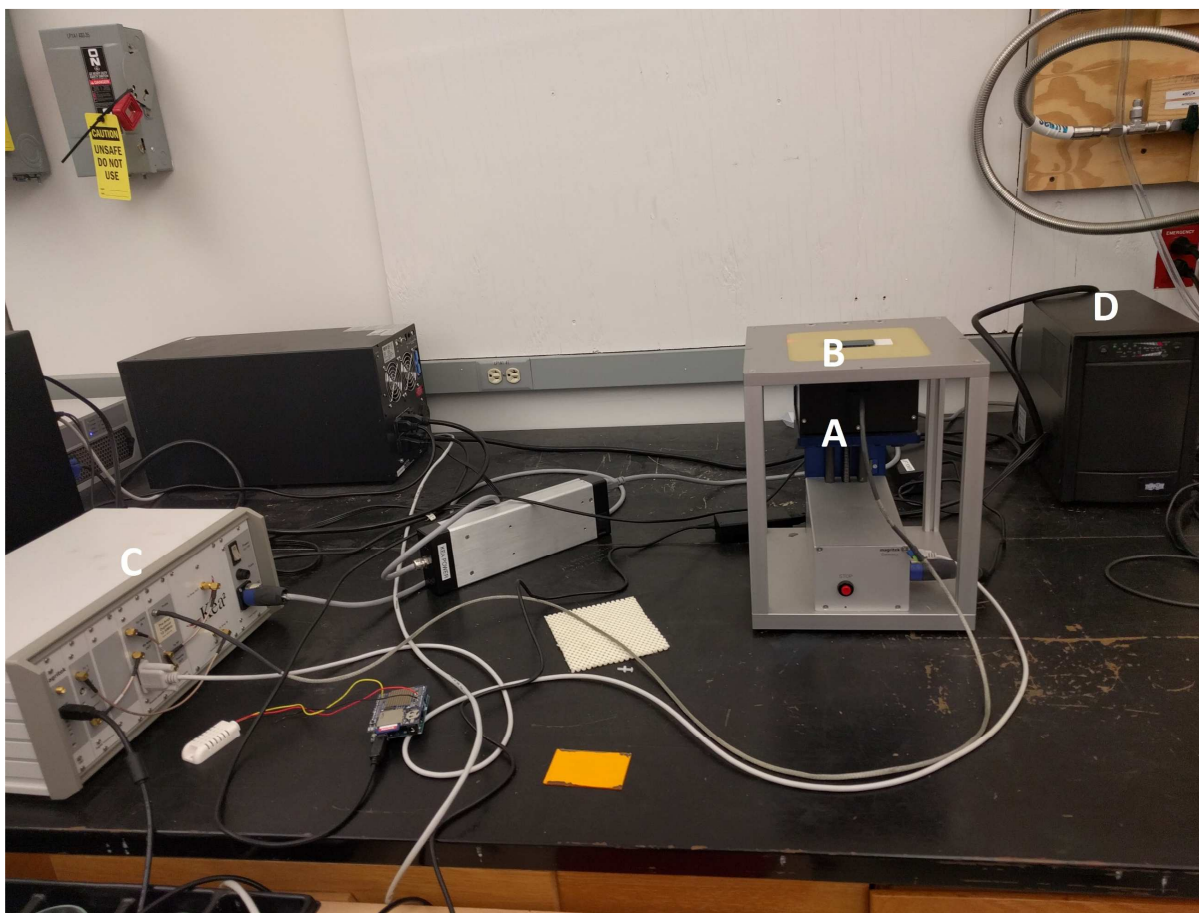


**Figure 14.** An image of the NMR-MOUSE apparatus used in our lab, including: (A) the magnet lift, (B) the sensing area for the magnet with a standard test sample, (C) the Kea Spectrometer used (Magritek), and (D) the backup power source. As seen in the image, the sample is placed directly on top of the magnet housing over the roughly 1 inch by 1 inch scanning area.

*Experimental parameters - profiles:*

CPMG experiments run over a range of depths were utilized to acquire the position of the sample with both the greatest signal and the signal corresponding to the sample of interest. Figures of the typical experimental parameters used in the Prospa software for a profile are in Appendix A. Once the experiment parameters have been set, a profile was run and the output profile was used for further experiments (Figure 15). The profiles run on Sample Group A consisted of two peaks in amplitude which were theorized to correspond to the canvas or wooden board support and a second merged peak corresponding to an area between the paint sample and the acrylic or traditional ground placed on the samples. The profiles run on Sample Groups B, C, and D, however, show one clear peak corresponding to just the paint or ARLO sample. It was significantly easier to find the area of signal for measurement in these samples.

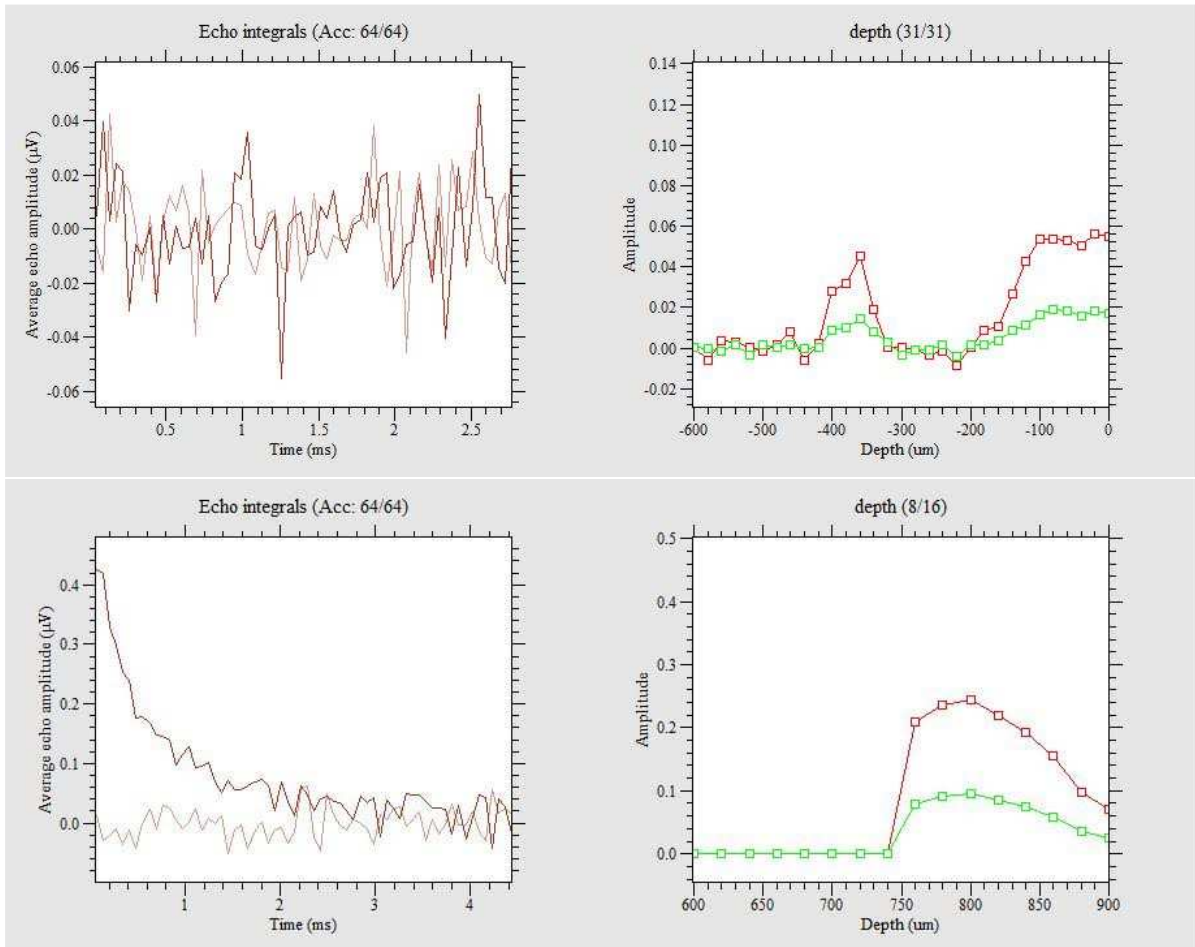


**Figure 15.** Sample profiles experiments for Sample Group A (top) and Sample Group B (bottom) as produced by the software Prospa (Magritek). In the Sample Group A profile, there are two peaks in amplitude in the plot to the right. These peaks correspond to the canvas to which the paint sample was affixed (–200 to 0 micron range) and the actual paint/ground sample itself (–320 to –440 micron range). Therefore, the magnet was moved to the position of –400 microns to measure at an area of strong signal corresponding to the paint itself. In the Sample Group B profile, there is a clear spike in amplitude that quickly drops off around the 750 micron depth. In order to measure these samples the magnet was moved to the 800 micron position, as it was the largest peak in the amplitude.

## CPMG experiments

Once the magnet had been properly positioned, standard CPMG experiments were run on the samples to determine the transverse relaxation times for each individual sample. The circles in Figure 16 depict some standard output data from the MATLAB script. The transverse relaxation values ultimately obtained through an exponential decay fit as shown in Figure 16.

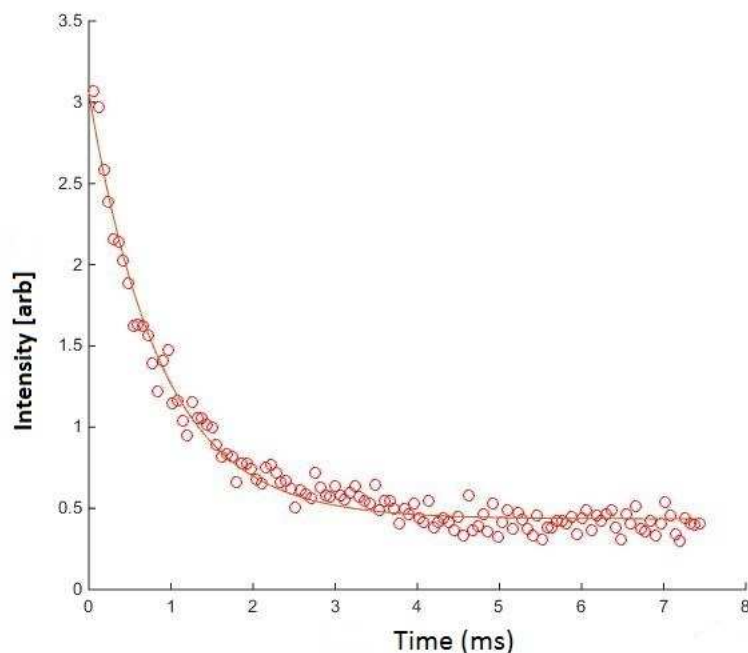


**Figure 16.** A plot of a standard echo decay train fit to an exponential decay curve. Each red circle corresponds to the amplitude of a single echo after the application of the refocusing pulse. The red curve going through the data is the exponential decay curve produced by the Matlab (Mathworks) script.



For Sample Groups B and C, CPMG measurements were made in increments of 20  $\mu\text{m}$  over a 400  $\mu\text{m}$  range, covering the entire thickness of the paint samples, in order to determine the area of greatest signal. Each measurement consisted of 64 scans at each position and lasted approximately 7 min. These measurements were made with a 4.75  $\mu\text{s}$  pulse for both the  $\pi/2$  and  $\pi$  pulses—the power of the  $\pi$  pulse was twice that of the  $\pi/2$  pulse. For each measurement, 64 echoes were collected with a 48  $\mu\text{s}$  echo time.

CPMG experiments were carried out on the area of paint providing the greatest signal as determined by measuring a one-dimensional depth profile. For Sample Groups B and C, the CPMG measurements were run with a pulse length ranging from 4.75 to 5.0  $\mu\text{s}$ , and 128 echoes were collected with an echo time of 60  $\mu\text{s}$ . Each measurement comprised 1024 acquisition scans for a total measurement time of 6.8 min. For Sample Group A, CPMG measurements were run with a pulse length of 2.75  $\mu\text{s}$ , and 128 echoes were collected with an echo time of 60  $\mu\text{s}$ . Each measurement comprised 1024 acquisition scans for a total measurement time of 5.1 min. The pulse length was reduced in this case because the samples in Group A are thinner than those in Groups B and C. Because these samples are thinner, a 2 mm thick plastic spacer was inserted underneath the rf coil, bringing it closer to the measurement region. Reducing the distance from the coil to the sample also reduces the power necessary for proper excitation. A table containing all the experiment parameters can be found in Appendix A.

### *Data processing*

Data processing was performed using MATLAB (The MathWorks Inc.; Natick, MA) and involved fitting the entire decay of the recorded echo train to an exponential decay curve of the form:

$$f(t) = y_0 + Ae^{-\frac{t}{T_2}}$$

where  $t$  is time in ms,  $y_0$  is the y-offset used to account for the signal not fully decaying and “edge-effects” of the data,  $A$  is the amplitude of the signal, and  $T_2$  is the transverse relaxation time. Built-in MATLAB functions were used to calculate a 90% confidence interval for each fit. Inverse Laplace transformations (ILTs) and exponential decay fits were both used to fit the data, however the decay fits provided more robust and consistent values for the  $T_2$  relaxation of the paint samples, and as such were chosen to represent the data. The exponential decay fit process involved removal of the first four echoes of data, followed by a mono-exponential fit of the echo decay train. Successful fits for the data were determined by analyzing the distribution of the residuals about zero, as shown in Figure 17. This procedure was used for all samples in every group in order to maintain a consistent data processing procedure. The Matlab scripts used for data processing are available in Appendix B.

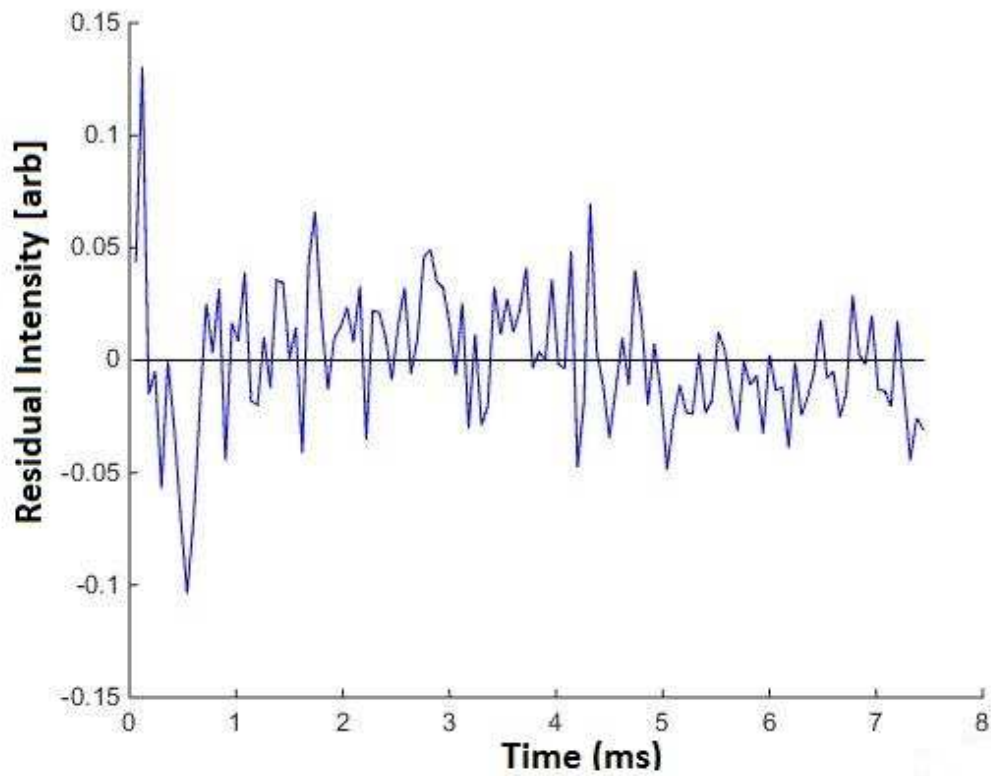


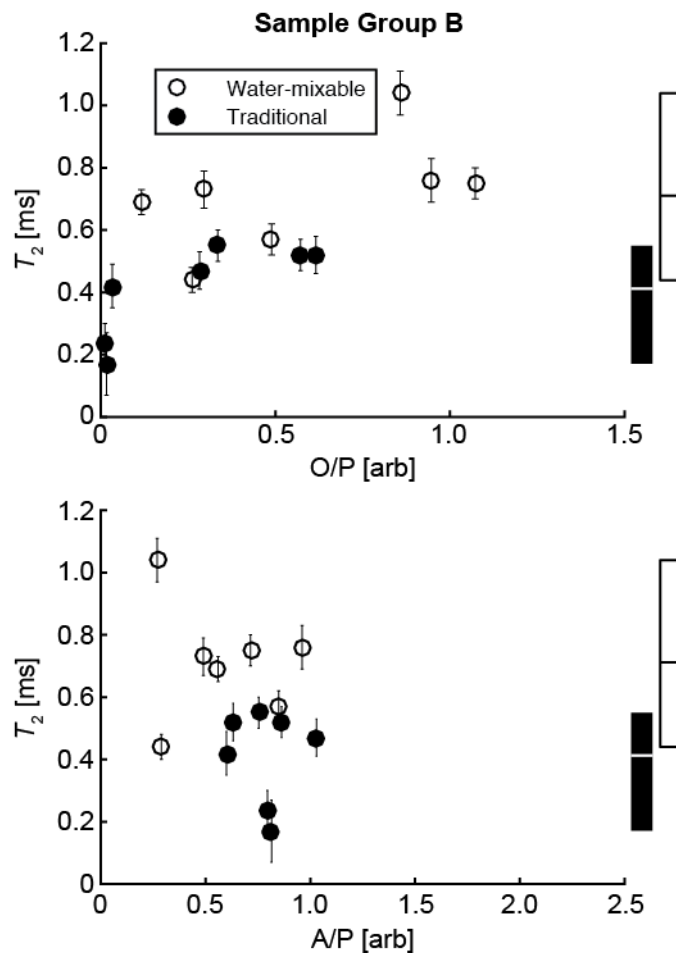
**Figure 17.** A typical residual plot used to confirm the success of a mono-exponential decay fit. The random distribution about 0 is evidence of a proper fit.

## **Chapter 4: Results and Discussion**

Numerical data for the relaxation values and fatty acid ratios obtained by GCMS are in Appendix B, in Tables 3–9.

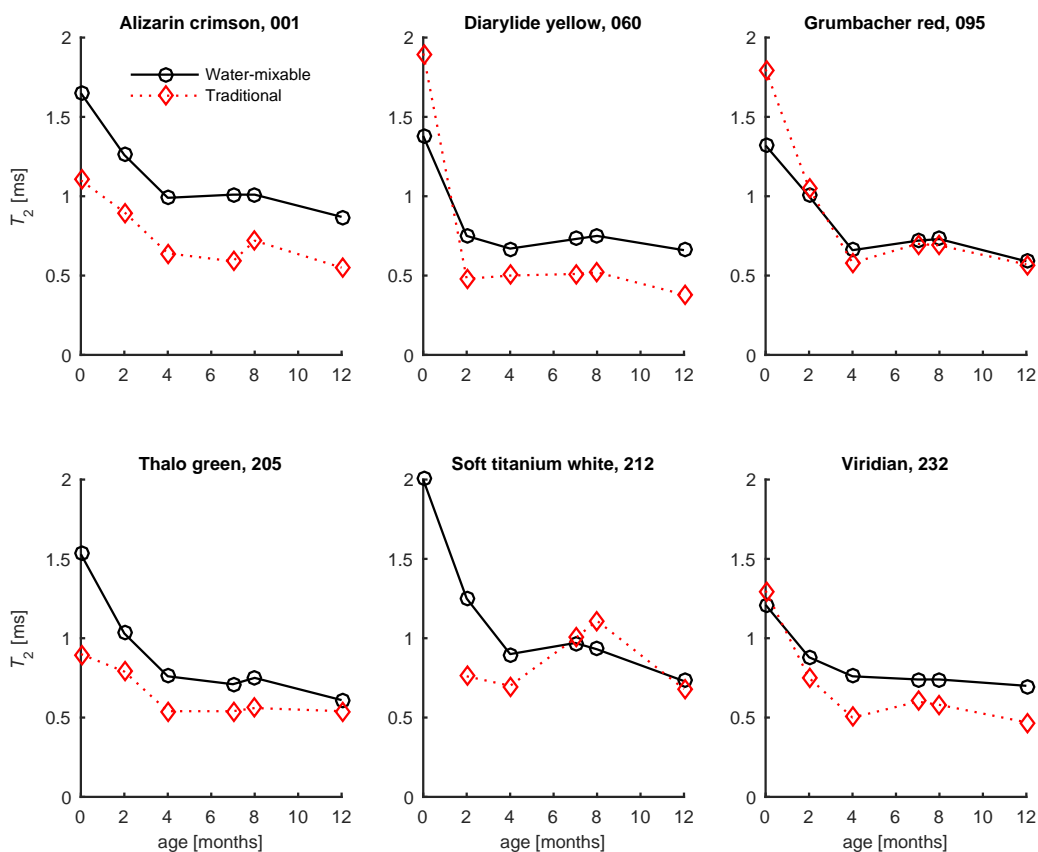
### *Sample Groups B and C*

Figure 18 compares relaxation times for Sample Group B against both the O/P ratio (top) and the A/P ratio (bottom) of the samples. A clear, positive correlation is observed between the O/P ratio and relaxation times. This suggests that the WMO samples not only have a different physical composition than the TOs (the WMOs having generally larger relaxation times), but also a different chemical composition, as indicated by the generally larger O/P ratio of the WMO samples. This observation supports the idea that the emulsifier interrupts both the physical network (relaxation) and the cross-linking process (O/P ratio) in the paint film. However, the A/P ratios of both WMOs and TOs span a significantly smaller range than do the O/P ratios. This suggests that the production of dicarboxylic acids has proceeded to a similar extent in samples both with and without the emulsifier. Thus, we hypothesize that the presence of the emulsifying agent causes two main effects in the WMO samples: (1) a change in the physical structure of the paint network, and (2) a relative slowing of the curing process. The emulsifying agent cross-links into the triglyceride paint network, directly inserting large POE chains. The presence of these POE chains allows for greater molecular motion within the samples, leading to larger observed relaxation values. The emulsifying agent is also able to slow down the curing of the WMOs relative to TOs: larger O/P ratios of the WMO samples indicate that less autoxidation has occurred. The production of azelaic acid depends on autoxidative curing:  $\beta$ -scission occurs either concurrently with or following autoxidation. The presence of a slightly lower A/P ratio on average for the WMO samples would in fact support the hypothesis of a reduced relative curing rate between the WMO and TO samples. The observation that the A/P ratio values are only slightly lower for the WMO samples serves as a reflection of the small amount of curing that has been able to occur in the time since the samples were measured.



**Figure 18.** Graph of the  $T_2$  relaxation times vs O/P fatty acid ratio (top) and A/P fatty acid ratio (bottom) for Sample Group B. The rectangles to the right of each plot indicate the range and average of each set of samples. There is a positive correlation between the O/P ratios and the relaxation times not noted in the A/P ratio figure. This correlation indicates that the presence of the emulsifying agent is slowing down the relative curing rate.

Figure 19 consists of the plots of relaxation values vs. cure time for selected paints in Sample Group C. Apart from a few outliers, WMO samples have larger relaxation values than their TO counterparts at all times during the first 12 months of curing. This supports the hypothesis that WMOs have different physical properties than TOs, at least at younger ages, but extends this hypothesis to early stages of curing.



**Figure 19.** Graph of  $T_2$  relaxation times versus the curing time that each sample has experienced in months (age) for Sample Group C. Each paint maintains the general trend of a greater relaxation time for WMO versus TO. The 0-month data point for TO pigment 212 was lost and as such is missing from the graph.

### *Sample Group A*

Like Figure 18, Figure 20 compares relaxation times for Sample Group A to both the O/P and A/P ratios of the samples. In contrast with younger samples, differences in physical properties between 20-year-old WMO and TO samples, as evaluated by NMR, are not nearly as large. However, the chemical compositions of the various samples seems to differ greatly across the pigment range. Excluding the three data points with the largest A/P ratios, a sharp negative correlation between relaxation values and the A/P ratio is present. Perhaps only in older paint samples is  $\beta$ -scission significant enough to produce measurable effects in physical properties of paint films. If one includes the three data points with high A/P ratios in this analysis, an apparent  $T_2$  “floor” is reached at approximately 0.3 ms. This may suggest that once a peak level of brittleness is achieved (with a low  $T_2$  value),  $\beta$ -scission may still convert unsaturated fatty acids into diacids, but the paint film will not become yet more brittle. In other words, these data may suggest that long-term changes in chemical composition will eventually have no effect on the physical composition of the samples. Similarly, there is no clear correlation between observed relaxation values and O/P ratios in Sample Group A—it is possible that physical brittleness of the paint film cause by autoxidation has reached a maximum value and that further decreases in the O/P ratio are no longer correlated with increased curing.

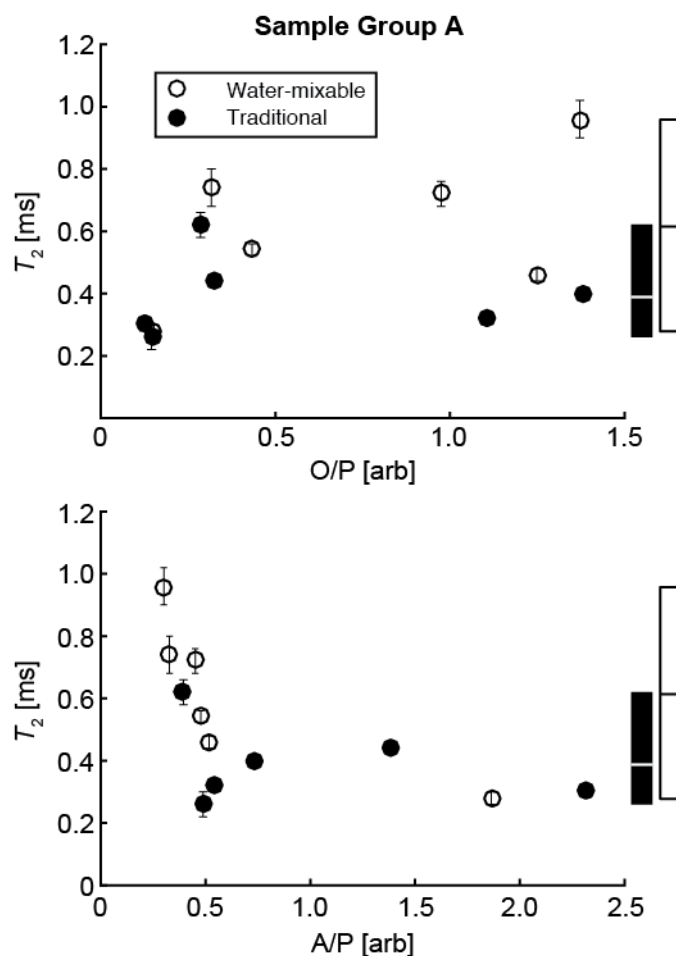


**Figure 20.** Graph of the O/P fatty acid ratios (top) and the A/P fatty acid ratios (bottom) vs the  $T_2$  relaxation times for Sample Group A. While the physical differences between the WMO and TO samples is not as large as for Sample Group B (see figure 18), there is still a clear trend of larger relaxation times for the WMO samples. In the O/P plot, there is a random distribution of ratios amongst the TO and WMO samples, not allowing for any substantial observation. However, disregarding the three largest A/P ratios, there is a strong negative correlation between A/P ratios and relaxation times.



### Sample Group D

In order to isolate complex effects from samples from real artists' paint, it was imperative to control data on samples containing only ARLO and the emulsifier (Atlas G-1086). Figure 21 plots relaxation values for these samples against both the O/P and A/P ratios. There are clear correlations between the relaxation values and both fatty acid ratios: higher concentrations of emulsifier decrease curing as measured by O/P (larger values indicate less curing) and A/P (smaller values indicate less curing). These data support our claims above, and suggest that the major effect is due to the emulsifier and not to other compounds in the paint mixture.

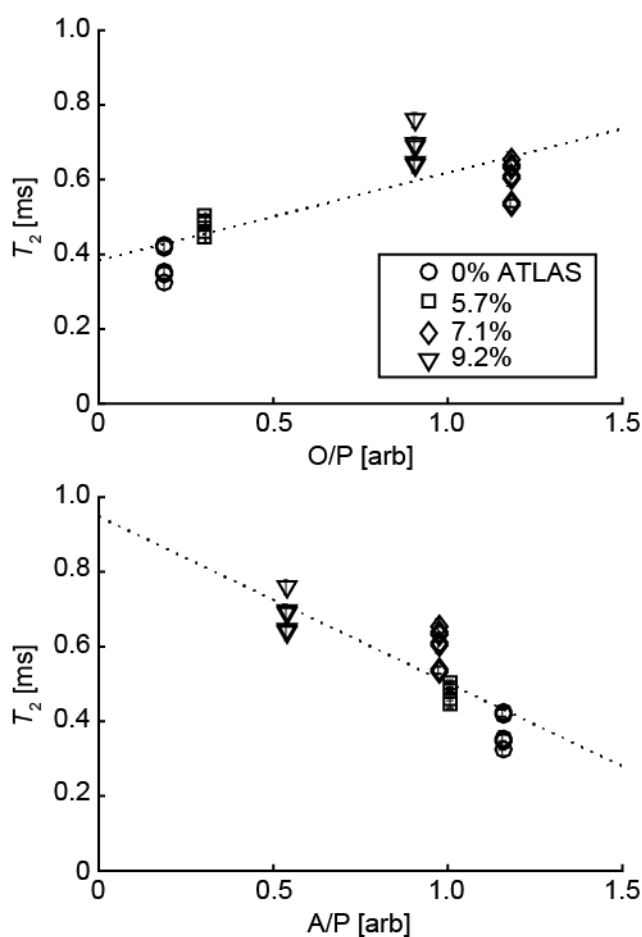


**Figure 21.** Graph of the  $T_2$  times vs O/P (top) and A/P (bottom) ratios for the ARLO and Atlas emulsifier only samples. The trends observed in Figures 18 and 20 are supported by this figure, indicating that the primary factor effecting the differences in  $T_2$  times is in fact the presence of greater concentrations of the emulsifying agent, which in turn increases the network size.

## **Conclusions:**

Despite some limitations of this research, primarily a small sample size, we have shown that complementary NMR and GCMS measurements can provide insight into the curing of paint films as measured by both chemical and physical properties. The research was relatively straightforward and required the greatest time investment on data collection. Comparing these two measurements shows that the addition of an emulsifier to oil paint reduces the rate of curing relative to a paint without emulsifier, and results in a less cross-linked paint film. This effect is consistent in both fresh and aged samples. However, access to samples across a more diverse range of ages would greatly benefit in determining thresholds for the effects of the emulsifying agent and relative curing trends. In addition, we hypothesize that even as chemical changes in paint films may continue for many decades, the extent of cross-linking as measured by NMR plateaus after some time, also lending to the need for a greater diversity in paint ages. Further inquiry into the temporal and chemical ranges over which this claim is valid is of merit.

The data collection posed issues that ended up requiring excessive amounts of time. Specifically, it would have been beneficial to ensure that the area of signal being measured in Sample Group A was in fact corresponding to the paint layer of the sample instead of the ground or support layers. Data acquisition on Sample Group A had to be repeated due to an error in finding the signal originally, in which the original data set had been taken on the acrylic and traditional grounds and not the paint layers themselves. Data processing performed involved an extensive amount of time and initial issues, as well. The samples in Sample Group C initially were fit better to a bi-exponential decay, but, after roughly four months of curing, they no longer seemed to have a bi-modal relaxation. More consistent and repeated data acquisitions within the first four months of curing would have greatly improved the ability to flesh out when the samples cure to a unimodal paint film. To eliminate inconsistencies in data processing, each sample was data processed in the same manor, as specified in the experimental section of this thesis. Elimination of the initial four echoes before fitting to a mono-exponential decay provided a consistent means of data processing that was acceptable in the fits provided.

Significant attention has been given recently to the mechanical properties of paint films (in contrast with chemical properties only), including the relative stress and strain effects on a paint film under varying temperature and relative humidity conditions.<sup>39</sup> Research has also been done into the structural composition of layered paint sample under varying humidity, temperature, solvent, and other conditions.<sup>40</sup> This report extends the utility of NMR relaxometry in evaluating paint films on a structural and physical basis. By combining numerous techniques and incorporating NMR data into research, the effects of multiple varying conditions on the brittleness and physical structure of a paint film can be clarified.

Several extensions of research are applicable to this specific project. As mentioned, the presence of a bi-exponential decay in fresh samples is evidence of two different components of the paints with separate relaxation times. Diffusion measurements currently being performed in lab may help explain the initial presence of the bi-modal relaxation, while also helping determine what species contribute to each individual relaxation mode. Extensive data collection was performed on Sample Group A samples, but GCMS data was only acquired by collaborators on the samples with an acrylic ground and canvas support. Moving GCMS in house would increase the speed with which data analysis could be done, while also eliminating the need for potentially confusing collaboration with other organizations. The ability to do GCMS in our research lab would also allow to perform data analysis and comparison of NMR and GCMS research on all of the samples in Sample Group A.

Outliers in these data sets may provide for other interesting lines of inquiry. First, the two samples with the largest A/P ratios in Sample Group A are the traditional and water-mixable paint with the pigment viridian. It is possible that viridian (chromium(III) oxide hydrate) itself has influenced the extent of  $\beta$ -scission in these samples. Furthermore, the two smallest A/P ratios come from the water mixable colors Grumbacher red and titanium white. These pigments are the only two WMO paints studied that have added zinc in their paint composition, capable of forming stearates. It is possible that zinc soap formation in paint films affects the chemical composition of these paints by inhibiting  $\beta$ -scission.

In addition to an exploration of the observed outliers, studies on other pigments and paints would allow for a larger data set that would increase the precision of the claims made here. Similarly, other samples similar to those in Sample Group A exist, though on wood panels (rather than canvas) or on a traditional oil ground (rather than an acrylic ground). A study of these samples may reveal effects of the ground and/or support onto which the paint is applied on the final physicochemical properties of the film.

# Appendix A – Tables

**Table 1. Profile Experimental Parameters**

	<b>Sample Group A</b>	<b>Sample Group B</b>	<b>Sample Group C</b>	<b>Sample Group D</b>
Spacer Addition (mm)	4	2	2	2
B <sub>1</sub> Frequency (MHz)	19.44	19.44	19.44	19.44
90 Amplitude (dB)	-10	-10	-10	-10
180 Amplitude (dB)	-4	-4	-4	-4
Pulse Length (μs)	5.0	4.5	4.5	4.5
Resolution (μm)	120	120	120	120
Repetition Time (ms)	400	300	300	300
Number of Scans	128	64	64	64
Number of Echoes	64	64	64	64
Initial Depth (μm)	0	900	900	1000
Final Depth (μm)	-600	600	600	600
Step Size (μm)	-20	-20	-20	-20

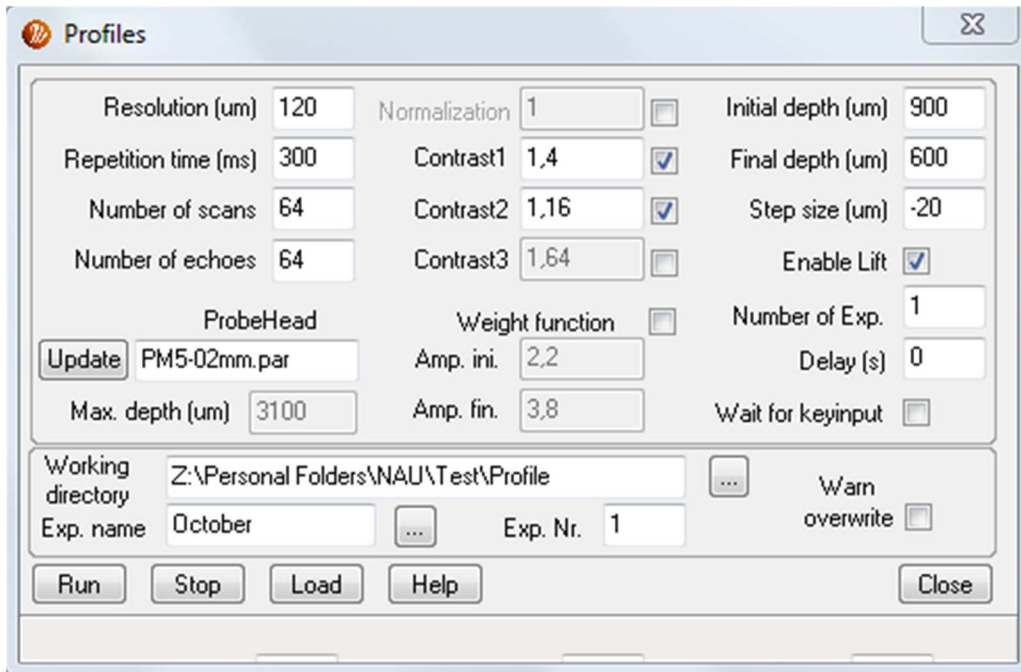
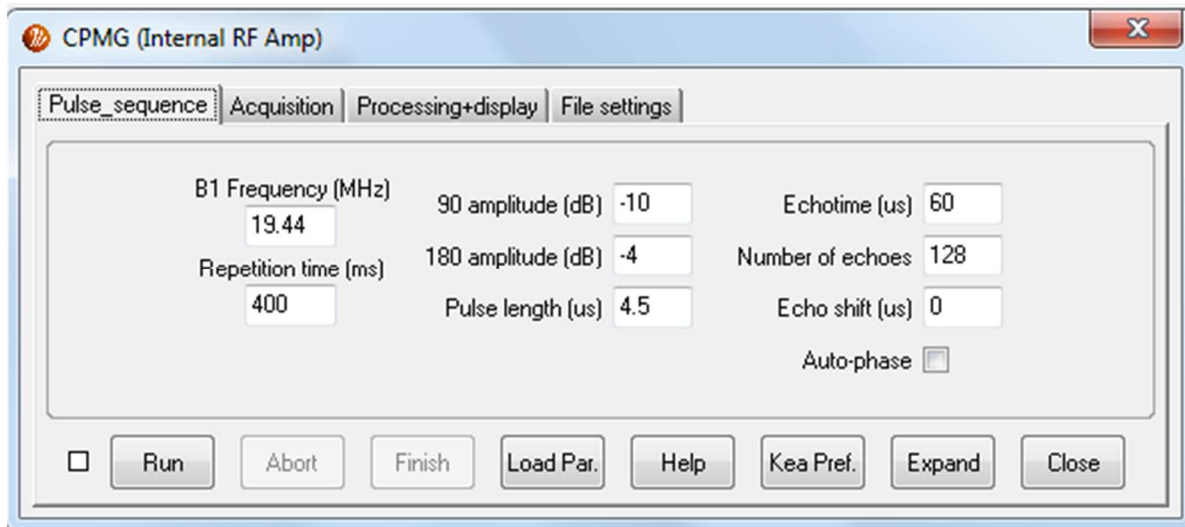
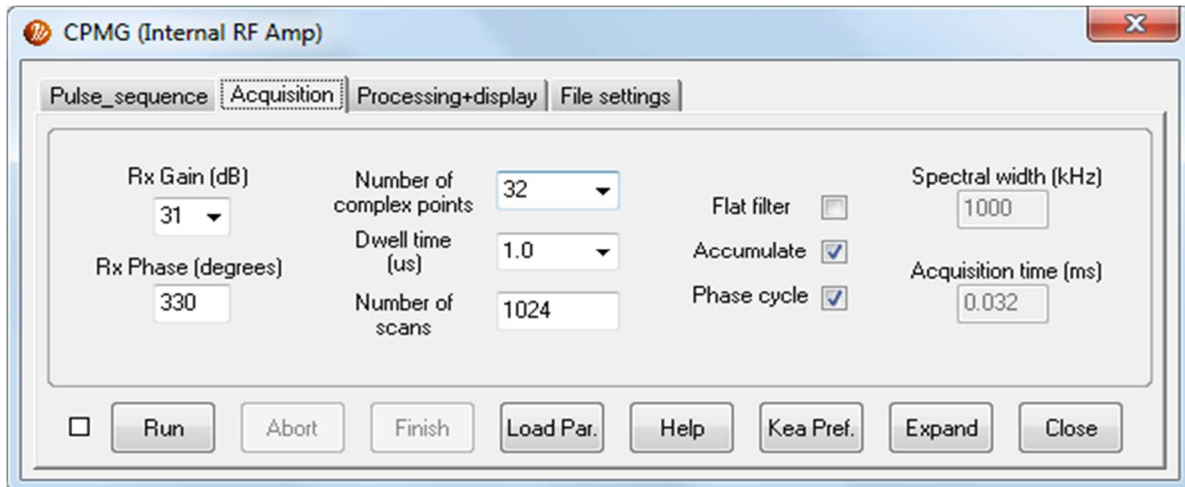


**Figure 22:** An example of the Prospa (Magritek) output parameters for a profile experiment on Sample Groups B, C, or D. Because all samples in these groups were relatively the same thickness, the profile was run from the same final to initial depth.

**Table 2. CPMG Experimental Parameters**

	<b>Sample Group A</b>	<b>Sample Group B</b>	<b>Sample Group C</b>	<b>Sample Group D</b>
Spacer Addition (mm)	4	2	2	2
B <sub>1</sub> Frequency (MHz)	19.44	19.44	19.44	19.44
90 Amplitude (dB)	-10	-10	-10	-10
180 Amplitude (dB)	-4	-4	-4	-4
Pulse Length ( $\mu$ s)	5.0	4.5	4.5	4.5
Echotime ( $\mu$ s)	60	60	60	60
Repetition Time (ms)	400	300	300	300
Number of Scans	1024	1024	1024	1024
Number of Echoes	128	128	128	128
Number of Complex Points	32	32	32	32
Dwell Time ( $\mu$ s)	1.0	1.0	1.0	1.0



**23:** Prospa output from a CPMG experiment run on Sample Groups B, C, and D with an altered 4.5 microsecond pulse length. Experiments run on these sample groups varied slightly from Sample Group A due to the presence or absence of additional spacers



**Table 3. Sample Group A Data**

<b>Pigment</b>	<b>Amplitude</b>	<b>Amplitude Error</b>	<b>T2</b>	<b>T2 Error</b>	<b>A/P</b>	<b>P/S</b>	<b>O/P</b>	<b>O/A</b>
M027	0.814811	0.029264	0.477381	0.027963	0.301	0.426	1.372	4.558
M060	0.974936	0.028499	0.36387	0.015857	0.451	0.523	0.976	2.161
M095	1.221193	0.037573	0.229752	0.009366	0.518	0.469	1.248	2.411
M205	1.001831	0.039027	0.268537	0.014424	0.478	0.667	0.434	0.907
M212	0.812391	0.039801	0.374746	0.027699	0.328	0.609	0.317	0.966
M232	1.444707	0.051917	0.143482	0.00607	1.863	1.13	0.153	0.082
P027	1.026454	0.134417	0.130035	0.019475	0.488	0.42	0.146	0.298
P060	1.002008	0.047428	0.218457	0.013577	1.388	0.345	0.324	0.233
P095	1.324554	0.052043	0.159704	0.007607	0.544	0.364	1.102	2.026
P205	1.123323	0.048177	0.201355	0.011093	0.731	0.813	1.384	1.894
P232	1.272561	0.066725	0.149749	0.009355	2.32	0.611	0.122	0.053
P250	0.9662	0.034865	0.314733	0.016283	0.395	0.635	0.286	0.724

**Table 4. Sample Group B Data**

Pigment	Amplitude	Amplitude Error	T2	T2 Error	A/P	P/S	O/P	O/A
M001	0.809627	0.046766	0.759814	0.069114	0.960728	0.856402	0.945967	0.984636
M027	0.821167	0.029935	1.038287	0.065904	0.269058	0.679066	0.857731	3.187909
M095	0.812967	0.053909	0.439636	0.041295	0.560138	0.66174	0.117246	0.209316
M060	0.863778	0.032235	0.693721	0.039889	0.289327	1.243851	0.261991	0.90552
M205	0.856756	0.037076	0.745276	0.050544	0.714843	0.889807	1.071994	1.499622
M212	0.767005	0.042817	0.726	0.063105	0.489685	0.895172	0.295655	0.603765
M232	0.792162	0.050244	0.573907	0.05396	0.849055	0.714869	0.488774	0.575669
P001	0.851211	0.061737	0.515866	0.054413	0.863439	0.657697	0.572049	0.662524
P027	0.652382	0.330334	0.16737	0.1014	0.814681	0.651896	0.016351	0.02007
P060	0.909803	0.07713	0.466266	0.056523	1.030362	0.777824	0.28288	0.274545
P095	0.82702	0.063703	0.524727	0.058952	0.632201	0.574381	0.616487	0.975143
P205	0.89384	0.059275	0.553904	0.054091	0.75355	0.789469	0.335597	0.445355
P232	0.812534	0.151466	0.235073	0.056125	0.795412	0.662772	0.012204	0.015343
P250	0.726319	0.081552	0.422814	0.066833	0.60013	0.782371	0.033799	0.05632

**Table 5. Sample Group C WMO Data (M001-M095)**

<b>Pigment</b>	<b>Age (months)</b>	<b>Amplitude</b>	<b>Amplitude Error</b>	<b>T2</b>	<b>T2 Error</b>
M001	0	0.766491	0.023928	1.64615	0.083928
M001	2	0.818298	0.022518	1.263412	0.066455
M001	4	0.87366	0.02756	0.994217	0.053685
M001	7	0.88883	0.027722	1.007261	0.054046
M001	8	0.873303	0.027749	1.011554	0.055386
M001	12	0.855385	0.030107	0.869649	0.050052
M027	0	0.73699	0.019207	2.523966	0.126111
M027	2	0.791159	0.02128	1.423412	0.07861
M027	4	0.820041	0.031208	1.17445	0.082244
M027	8	0.802207	0.023639	1.245758	0.069631
M027	12	0.809725	0.029224	1.06602	0.067725
M060	0	0.771683	0.024838	1.380608	0.069755
M060	2	0.834158	0.04295	0.748176	0.08202
M060	4	0.916939	0.033467	0.670857	0.037448
M060	7	0.876122	0.032269	0.732514	0.042103
M060	8	0.872968	0.032455	0.74595	0.043471
M060	12	0.857558	0.042582	0.658927	0.049847
M095	0	0.726782	0.025951	1.31823	0.092162
M095	2	0.808579	0.026277	0.997929	0.055595
M095	4	0.889978	0.03744	0.659679	0.04229
M095	7	0.854741	0.040585	0.721184	0.053241
M095	8	0.8455	0.037606	0.730952	0.050711
M095	12	0.853558	0.04614	0.594209	0.047927

**Table 6. Sample Group C WMO Data (M205-M232)**

<b>Pigment</b>	<b>Age (months)</b>	<b>Amplitude</b>	<b>Amplitude Error</b>	<b>T2</b>	<b>T2 Error</b>
M205	0	0.763927	0.023128	1.526835	0.074128
M205	2	0.819326	0.025925	1.034523	0.056913
M205	4	0.877413	0.039892	0.763587	0.054739
M205	7	0.894688	0.033243	0.711549	0.040973
M205	8	0.919142	0.03184	0.74946	0.040741
M205	12	0.909573	0.043717	0.60883	0.043869
M212	0	0.731728	0.023346	1.97057	0.108367
M212	2	0.794537	0.028142	1.248883	0.084021
M212	4	0.803981	0.041624	0.897529	0.076748
M212	7	0.832196	0.034488	0.965617	0.067765
M212	8	0.853959	0.033099	0.925356	0.059836
M212	12	0.789316	0.050638	0.733152	0.073413
M232	0	0.799067	0.02444	1.210591	0.056764
M232	2	0.829331	0.028351	0.882862	0.049586
M232	4	0.85834	0.041223	0.756926	0.057188
M232	7	0.865951	0.028898	0.742573	0.038798
M232	8	0.906954	0.027325	0.742077	0.034999
M232	12	0.8413	0.040309	0.703516	0.052103

**Table 7. Sample Group C TO Data (P001-P095)**

<b>Pigment</b>	<b>Age (months)</b>	<b>Amplitude</b>	<b>Amplitude Error</b>	<b>T2</b>	<b>T2 Error</b>
P001	0	0.728819	0.036968	1.120856	0.102309
P001	2	0.835419	0.032102	0.899985	0.057165
P001	4	0.877014	0.044191	0.636259	0.048491
P001	7	0.903572	0.047394	0.594908	0.04657
P001	8	0.913018	0.035431	0.723975	0.04372
P001	12	0.839995	0.052049	0.550277	0.050156
P027	0	0.636486	0.017566	2.051711	0.153886
P027	2	0.784609	0.043533	0.780359	0.068647
P027	4	0.815757	0.059896	0.449764	0.046949
P027	7	0.763802	0.108989	0.376132	0.074195
P027	8	0.827651	0.07108	0.492887	0.061091
P027	12	0.773902	0.071834	0.4823	0.064376
P060	0	0.670214	0.02039	1.868805	0.143149
P060	2	0.799886	0.054156	0.482642	0.044923
P060	4	0.866185	0.059704	0.504075	0.050332
P060	7	0.804004	0.054205	0.509857	0.049893
P060	8	0.897693	0.051868	0.519408	0.043699
P060	12	0.844431	0.080005	0.379229	0.049734
P095	0	0.667969	0.02415	1.756123	0.151996
P095	2	0.795841	0.032208	1.054671	0.074798
P095	4	0.866354	0.04898	0.580693	0.048774
P095	7	0.826495	0.043825	0.700032	0.057313
P095	8	0.865196	0.037431	0.688901	0.045849
P095	12	0.760029	0.056441	0.568444	0.062465

**Table 8. Sample Group C TO Data (P205-P250)**

<b>Pigment</b>	<b>Age (months)</b>	<b>Amplitude</b>	<b>Amplitude Error</b>	<b>T2</b>	<b>T2 Error</b>
P205	0	0.75153	0.034853	0.928734	0.109542
P205	2	0.825726	0.033681	0.788752	0.051157
P205	4	0.886972	0.05157	0.539099	0.04594
P205	7	0.963597	0.040814	0.544201	0.033839
P205	8	0.874848	0.038467	0.555364	0.03598
P205	12	0.824605	0.056802	0.539916	0.054523
P212	2	0.811451	0.045334	0.76408	0.067319
P212	4	0.764609	0.068759	0.731212	0.102566
P212	7	0.753453	0.043608	1.002366	0.099611
P212	8	0.76098	0.039135	1.116944	0.103208
P212	12	0.754589	0.067914	0.676597	0.093305
P232	0	0.749957	0.030256	1.271266	0.09837
P232	2	0.783501	0.045451	0.753683	0.068707
P232	4	0.805265	0.07042	0.497647	0.062911
P232	7	0.880709	0.038242	0.601682	0.039077
P232	8	0.950024	0.038538	0.576027	0.03466
P232	12	0.819808	0.069455	0.467408	0.056651
P250	0	0.783083	0.030859	1.15788	0.08338
P250	2	0.812512	0.036998	0.771142	0.055507
P250	4	0.869284	0.048383	0.635745	0.053509
P250	7	0.865552	0.044661	0.649439	0.050898
P250	8	0.912434	0.040585	0.628025	0.042136
P250	12	0.686314	0.069347	0.551286	0.081965

**Table 9. Sample Group D Data**

Sample	Expt #	A	A Error	T2	T2 Error	A/P	P/S	O/P	O/A
Utrekt Akali	1	0.51809	0.058609	0.417511	0.066343	1.156	1.177	0.188	0.162
Utrekt Akali	2	0.77309	0.040181	0.465606	0.034593	1.156	1.177	0.188	0.162
Utrekt Akali	3	0.933614	0.021901	0.423898	0.014004	1.156	1.177	0.188	0.162
Utrekt Akali	4	0.980722	0.019143	0.420323	0.011538	1.156	1.177	0.188	0.162
Utrekt Akali	5	0.963766	0.031383	0.355378	0.015856	1.156	1.177	0.188	0.162
Utrekt Akali	6	0.916649	0.031484	0.342887	0.016047	1.156	1.177	0.188	0.162
Utrekt Akali	7	0.972233	0.039575	0.328392	0.018093	1.156	1.177	0.188	0.162
Utrekt Average		0.865452	0.034611	0.393428	0.025211	1.156	1.177	0.188	0.162
Atlas in ARLO 5.7	1	0.982712	0.016922	0.4814	0.011916	1.006	1.151	0.306	0.304
Atlas in ARLO 5.7	2	1.009506	0.016357	0.490748	0.011467	1.006	1.151	0.306	0.304
Atlas in ARLO 5.7	3	0.971963	0.015531	0.501041	0.011586	1.006	1.151	0.306	0.304
Atlas in ARLO 5.7	4	0.909514	0.021866	0.481342	0.016634	1.006	1.151	0.306	0.304
Atlas in ARLO 5.7	5	0.994655	0.023117	0.458976	0.015214	1.006	1.151	0.306	0.304
Atlas in ARLO 5.7	6	0.952899	0.020338	0.444679	0.013468	1.006	1.151	0.306	0.304
Atlas in ARLO 5.7	7	0.991299	0.023532	0.463478	0.015717	1.006	1.151	0.306	0.304
5.7 Average		0.973221	0.019666	0.474523	0.013715	1.006	1.151	0.306	0.304
Atlas in ARLO 7.1	1	0.936009	0.016382	0.538635	0.013814	0.972	1.203	1.179	1.213
Atlas in ARLO 7.1	2	0.966057	0.015099	0.535271	0.012245	0.972	1.203	1.179	1.213
Atlas in ARLO 7.1	3	0.899664	0.01568	0.611059	0.015977	0.972	1.203	1.179	1.213
Atlas in ARLO 7.1	4	0.891344	0.016033	0.632073	0.017172	0.972	1.203	1.179	1.213
Atlas in ARLO 7.1	5	0.904399	0.015075	0.642804	0.016239	0.972	1.203	1.179	1.213
Atlas in ARLO 7.1	6	0.910616	0.016291	0.60236	0.01612	0.972	1.203	1.179	1.213
Atlas in ARLO 7.1	7	0.897272	0.015294	0.65441	0.016969	0.972	1.203	1.179	1.213
7.1 Average		0.915052	0.015693	0.602373	0.015505	0.972	1.203	1.179	1.213
Atlas in ARLO 9.2	1	0.913501	0.016269	0.643605	0.017376	0.536	1.52	0.904	1.686
Atlas in ARLO 9.2	2	0.922265	0.015286	0.637121	0.015975	0.536	1.52	0.904	1.686
Atlas in ARLO 9.2	3	0.90318	0.014934	0.693044	0.017652	0.536	1.52	0.904	1.686
Atlas in ARLO 9.2	5	0.914227	0.014565	0.692658	0.016997	0.536	1.52	0.904	1.686
Atlas in ARLO 9.2	6	0.89127	0.013865	0.693878	0.016632	0.536	1.52	0.904	1.686
Atlas in ARLO 9.2	7	0.894559	0.01463	0.75906	0.019544	0.536	1.52	0.904	1.686
9.2 Average		0.9065	0.014925	0.686561	0.017363	0.536	1.52	0.904	1.686

## Appendix C – Definition of Acquisition Parameter Terms

1. -90/-180 Amplitude (dB): The power of the on-resonance excitation and refocusing pulses, respectively.
2. Pulse Length ( $\mu\text{s}$ ): Abbreviated as  $\tau$ , this value indicates the length of each magnetic pulse applied. The value for the specific pulse length is calibrated periodically via a calibration test and varies with the number of spacers in.
3. Repetition Time (ms): The time between the acquisition of the echo and the repetition of another scan via another refocusing pulse. The rep. time is typically thought of as the length of an entire scan and is primarily used to determine the whole length of an experiment.
4. Number of Scans: The number of defined pulse sequences used in the CPMG experiments. An increase in the total scans increases the overall signal, as more signal amplitudes are summed. However, the increase in scans also increases the length of an experiment.
5. Number of Echoes: The number of echoes acquired per each scan. Samples with longer relaxation times require more echoes in order to capture the entire signal decay.
6. Echotime ( $\mu\text{s}$ ): The length of time through which each echo is acquired, including the application of the refocusing pulse. The number of echoes multiplied by the echo time roughly equalates to the length of a single scan.
7. Number of Complex Points: The total amount of “collections” per each echo. When multiplied by the dwell time, the acquisition time for a single echo can be calculated.
8. Dwell Time ( $\mu\text{s}$ ): The amount of time per each complex point acquisition. When multiplied by the number of complex points, the acquisition for a single echo can be calculated
9. Depth ( $\mu\text{m}$ ): The position at which the NMR MOUSE is acquiring data. The initial depth in a profile is the higher position of the magnet and the final depth is the position that the magnet is lowered to.



## **Appendix D - Abbreviations**

ARLO – Atlas-Refined Linseed Oil

CPMG – Carr-Purcell-Meiboom Gill Pulse Experiment

FID – Free-Induction Decay

GCMS – Gas Chromatography – Mass Spectrometry

MOUSE – Mobile Universal Surface Explorer

NMR – Nuclear Magnetic Resonance (Spectroscopy)

POE – Polyethoxyethylene

RF - Radiofrequency

TO – Traditional Oil Paints

WMO – Water-Miscible Oil Paints

## Appendix E – MATLAB Script

Note: This script calls another smaller fitting function titled “monodecay\_t2fit” which calls the fitting function “t2monofit.” “monodecay\_t2fit” uses the guesses provided to provide an output fit with coefficients, residual values, and a Jacobian used to produce predicted fits for the data. These scripts are the actual fitting parameter being used.

```
clear
clc
close all

% Save Output Parameters

pigment = 'P250';
age = '0';
support = 'Glass';

% Get Experimental Parameters and Name output final data location
parfilestem = ('Z:\Personal Folders\NAU\insert file location here');
finalDataFile = 'Z:\Personal Folders\NAU\Processed Data\T2MonoData.csv';

file1      = ('Z:\Personal Folders\NAU\Raw Data\insert file location here\');

params.acqTime = readpar_Kea(strcat(parfilestem, '.par'), 'acqTime');
params.bandwidth = readpar_Kea(strcat(parfilestem, '.par'), 'bandwidth');
params.nrScans = readpar_Kea(strcat(parfilestem, '.par'), 'nrScans');
params.rxPhase = readpar_Kea(strcat(parfilestem, '.par'), 'rxPhase');
params.rxGain = readpar_Kea(strcat(parfilestem, '.par'), 'rxGain');
params.nrPts = readpar_Kea(strcat(parfilestem, '.par'), 'nrPnts');
params.repTime = readpar_Kea(strcat(parfilestem, '.par'), 'repTime');
params.repTime = readpar_Kea(strcat(parfilestem, '.par'), 'repTime');
params.blFreq = readpar_Kea(strcat(parfilestem, '.par'), 'blFreq');
params.nrEchoes = readpar_Kea(strcat(parfilestem, '.par'), 'nrEchoes');
params.echoTime = readpar_Kea(strcat(parfilestem, '.par'), 'echoTime');

fitopts = statset('MaxIter', 5000, 'TolX', 1e-14, 'UseParallel', true, 'Display', 'off');

% Datafile1
data1 = load(strcat(file1, 'data2.csv')); % Open datafile
data1 = reshape(data1, 2, params.nrEchoes*params.nrPts);

% Separate data into real and imaginary components
dataRe = data1(1, :);
dataIm = data1(2, :);

% Complex data into a real, imaginary format
dataCp = complex (dataRe, dataIm);
dataCp = reshape(dataCp, params.nrPts, params.nrEchoes);

% add in "abs" part to account for "edge" effects in echo shapes-- absolute
```

```

% value mode also requires a y-offset in fitting
data1d = sum(abs(dataCp),1);

% Set data to remove first four echoes
data1d = data1d(:,5:end);
% Time vector to match the removal of the four echoes
echoVec = (1:params.nrEchoes-4)*params.echoTime*1e-06;

% FITS
omit_Points = 0;
echotime = data1(:,1);

% Insert guesses for exponential decay fit

y0_guess = 0.1;
A_guess = .5;
t2_guess = 2.75e-04;
t2_guess2 = .003; %s

% Load guesses
guesses = [y0_guess;A_guess;t2_guess]

CI = 90; %desired confidence interval in percent
fitdata = real(data1d);

% Choose between bi-exponential and mono-exponential decay. Our data is all
% produced by a mono-exponential decay

[xfit,ypred,coeffs,coeff_err,residuals,se] =
monodecay_t2fit(echoVec,fitdata./max(fitdata),guesses,CI,fitopts);

%[xfit,ypred,coeffs,coeff_err,residuals,se] =
bidecay_t2fit(echoVec,fitdata./max(fitdata),guesses,CI,fitopts);

% Save output data in finalDataFile
fid = fopen(finalDataFile,'a+');
fprintf(fid, '%s,%s,%s,%s,%s,%s,%i,%f,%f,%f,%f, \n', date, file1, pigment, age, substrateground,
params.echoTime,coeffs(2),coeff_err(2),1000*coeffs(3),1000*coeff_err(3));
fclose(fid);

% Plot echo train with exponential decay fit
figure(1)
hold on
scatter(echotime(omit_Points+1:end),amplitude(omit_Points+1:end,1),'or')
scatter(echoVec,real(data1d),'or')
plot(xfit,ypred.*max(fitdata))
plot(xfit,[coeffs(1)+coeffs(2)*exp(-xfit./coeffs(3))].*max(fitdata),'b')
xlabel('ms')
ylabel('signal amplitude')

% Plot residual plot to confirm success of mono-exponential decay
figure(2)
hold on

```

```
plot(echovec, residuals, '-b')  
line([0,max(echovec)], [0,0])  
plot(echovec, zeros(length(residuals)), '-k')  
text(0.4*max(xfit), 0.8*max(ypred), textinfo)'
```

## Bibliography

- (1) Ning, Y.-C. *Struct. Identif. Org. Compd. with Spectrosc. Tech.* **2005**, *17*, 1–26.
- (2) Eidmann, G.; Savelsberg, R.; Blümmler, P.; Blümich, B. *J. Magn. Reson. Ser. A* **1996**, *122* (1), 104–109.
- (3) Kleinberg, R. L.; Jackson, J. a. *Concepts Magn. Reson.* **2001**, *13* (6), 340–342.
- (4) Kleinberg, R. L. *Concepts Magn. Reson.* **2001**, *13* (June), 342–343.
- (5) Musse, M.; Cambert, M.; Mariette, F. *Appl. Magn. Reson.* **2010**, *38* (4), 455–469.
- (6) Marigheto, N.; Venturi, L.; Hills, B. *Postharvest Biol. Technol.* **2008**, *48* (3), 331–340.
- (7) Marigheto, N.; Duarte, S.; Hills, B. P. *Appl. Magn. Reson.* **2005**, *29* (4), 687–701.
- (8) Anferova, S.; Anferov, V.; Adams, M.; Fechete, R.; Schroeder, G. **2004**, *370*, 361–370.
- (9) Del Federico, E.; Centeno, S. A.; Kehlet, C.; Currier, P.; Stockman, D.; Jerschow, A. *Anal. Bioanal. Chem.* **2010**, *396* (1), 213–220.
- (10) Ulrich, K.; Centeno, S. A.; Arslanoglu, J.; Del Federico, E. *Prog. Org. Coatings* **2011**, *71* (3), 283–289.
- (11) Fife, G. R.; Stabik, B.; Kelley, A. E.; King, J. N.; Blümich, B.; Meldrum, T. **2015**, No. April 2014, 58–63.
- (12) Haber, A.; Blümich, B.; Souvorova, D.; Del Federico, E. *Anal. Bioanal. Chem.* **2011**, *401* (4), 1441–1452.
- (13) Proietti, N.; Capitani, D.; Rossi, E.; Cozzolino, S.; Segre, A. L. *J. Magn. Reson.* **2007**, *186* (2), 311–318.
- (14) Blumich, B.; Casanova, F.; Perlo, J.; Presciutti, F.; Anselmi, C.; Doherty, B. *Acc. Chem. Res.* **2010**, *43* (6), 761–770.
- (15) Terenzi, C.; Casieri, C.; Felici, A. C.; Piacentini, M.; Vendittelli, M.; De Luca, F. *J. Archaeol. Sci.* **2010**, *37* (7), 1403–1412.
- (16) Proietti, N.; Capitani, D.; Pedemonte, E.; Blümich, B.; Segre, A. L. *J. Magn. Reson.* **2004**, *170* (1), 113–120.
- (17) Blümich, B.; Anferova, S.; Sharma, S.; Segre, A. L.; Federici, C. *J. Magn. Reson.* **2003**, *161* (2), 204–209.
- (18) Sharma, S.; Casanova, F.; Wache, W.; Segre, A.; Blümich, B. *Magn. Reson. Imaging* **2003**, *21* (3–4), 249–255.
- (19) Perlo, J.; Casanova, F.; Blümich, B. *J. Magn. Reson.* **2005**, *176* (1), 64–70.
- (20) Meiboom, S.; Gill, D. *Rev. Sci. Instrum.* **1958**, *29* (8), 688–691.

- (21) H. Carr, E. Purcell, *Phys. Rev.* 1954-05, 94, 630–638.
- (23) Schilling, M.; Mazurek, J.; Learner, T. J. S. Studies of Modern Oil-Based Artists' Paint Media by Gas Chromatography/Mass Spectrometry. In: Learner T, Smithen P, Krueger JW, Schilling MR, editors. *Modern Paints Uncovered: Proceedings from the Modern Paints Uncovered Symposium, May 16-19, 2006, Tate Modern, London.* London: The Getty Conservation Institute; 2007. p. 129-139. (24) Keeler, J. *SpringerReference* **2002**, No. December, 211.
- (25) Hahn, E. L. *Phys. Rev.* **1950**, 77 (2), 297–298.
- (26) Blümich, B.; Blümler, P.; Eidmann, G.; Guthausen, A.; Haken, R.; Schmitz, U.; Saito, K.; Zimmer, G. *Magn. Reson. Imaging* **1998**, 16 (5–6), 479–484.
- (27) Hahn, E. L. *Phys. Rev.* **1950**, 80 (4), 580–594.
- (28) Casanova, F.; Perlo, J.; Blümich, B. *Single-sided NMR*; 2011.
- (29) Heydenreich, G. **2014**, No. march, 430.
- (30) Van Gorkum, R.; Bouwman, E. In *Coordination Chemistry Reviews*; 2005.
- (31) Soucek, M. D.; Khattab, T.; Wu, J. *Prog. Org. Coatings* **2012**.
- (32) Heydenreich, G. **2014**, No. January 2014, 430.
- (33) Mallégol, J.; Gardette, J.-L.; Lemaire, J. *J. Am. Oil Chem. Soc.* **1999**, 76 (8), 967–976.
- (34) Lazzari, M.; Chiantore, O. *Polym. Degrad. Stab.* **1999**, 65 (2), 303–313.
- (35) Colombini, M. P.; Modugno, F.; Giacomelli, M.; Francesconi, S. *J. Chromatogr. A* **1999**, 846 (1–2), 113–124.
- (36) Mills, J. S. **2016**, 11 (2), 92–107.
- (37) Bonaduce, I.; Carlyle, L.; Colombini, M. P.; Duce, C.; Ferrari, C.; Ribechini, E.; Selleri, P.; Tiné, M. R. *PLoS One* **2012**, 7 (11).
- (38) Oakley, L. H.; Casadio, F.; Shull, K. R.; Broadbelt, L. J. *Appl. Phys. A Mater. Sci. Process.* **2015**, 121 (3), 869–878.
- (39) Mecklenburg, M. F.; Tumosa, C. S. *Ashrae* **1999**, 41 (4), 69–74.
- (40) Mecklenburg Marion F. *Smithson. Museum Conserv. Institute.* **2007**, 1–29.